VALIDATION OF THE AFIT SMALL SCALE COMBUSTION FACILITY AND OH LASER-INDUCED FLUORESCENCE OF AN ATMOSPHERIC LAMINAR PREMIXED FLAME

THESIS

Stephen J. Koether, Second Lieutenant, USAF

AFIT/GAE/ENY/07-S03

DEPARTMENT OF THE AIR FORCE
AIR UNIVERSITY
AIR FORCE INSTITUTE OF TECHNOLOGY

Wright-Patterson Air Force Base, Ohio

The views expressed in this thesis are those of the author and do not reflect the official policy or position of the United States Air Force, Department of Defense, or the United States Government.

AFIT/GAE/ENY/07-S03

VALIDATION OF THE AFIT SMALL SCALE COMBUSTION FACILITY AND OH LASER-INDUCED FLUORESCENCE OF AN ATMOSPHERIC LAMINAR PREMIXED FLAME

THESIS

Presented to the Faculty

Department of Aeronautics and Astronautics

Graduate School of Engineering and Management

Air Force Institute of Technology

Air University

Air Education and Training Command

In Partial Fulfillment of the Requirements for the

Degree of Master of Science in Aeronautical Engineering

Stephen J. Koether, BS

Second Lieutenant, USAF

September 2007

AFIT/GAE/ENY/07-S03

VALIDATION OF THE AFIT SMALL SCALE COMBUSTION FACILITY AND OH LASER-INDUCED FLUORESCENCE OF AN ATMOSPHERIC LAMINAR PREMIXED FLAME

Stephen J. Koether, BS
Second Lieutenant, USAF

Approved:

//signed//	31 Aug 07
Paul King	date
//signed//	31 Aug 07
Richard Branam	date
//signed//	31 Aug 07
Mark Reeder	date

AFIT/GAE/ENY/07-S03

Abstract

Construction in the AFIT combustion facility is complete and the objective of this report is to explain the steps taken to make the laboratory operational. The infinite radius Ultra-Compact Combustor (UCC) sectional model has been delivered and is fully installed with all fuel, air and instrument lines. Every major system in the lab has been tested and is functioning properly. Laboratory operating procedure has been established to ensure both safety and continuity in experimental results. Finally, the lab has been certified through official safety channels and combustion experiments are underway. The unique capability of the AFIT combustion laboratory is the laser diagnostic system. The laser system has been configured for OH Laser-Induced Fluorescence (LIF) and initial experiments were performed on a premixed, laminar flame produced by a Hencken burner. The LIF methods accurately measured the OH concentration and temperature of the flame as compared to theoretical equilibrium flame data with an overall system uncertainty of approximately 2.5%. Therefore, the laser system has been calibrated and is ready for future use.

Acknowledgements

First and foremost I would like to thank my wife for all of the love and support that she has given me over the last year. She deserves most of the credit for me completing this 12 month program. From taking care of everything around the house to helping me with work in the lab, she truly has done it all. I would also like to thank my parents for the work ethic they have instilled in me and for all of the phone calls of support and love over the last year.

I would like to thank my advisor, Dr. Paul King, for his advice and direction. I also owe a great bit of gratitude to Dr. Richard Branam who oversaw the day to day activities in the combustion facility and helped me every step of the way. A very special thanks to John Hixenbaugh for his technical know-how and ability to get things done.

Thank you to Dr. Sukesh Roy and Dr. Terry Meyer for being patient with me as you taught me the basics of laser spectroscopy. Finally, Keith Grinstead has been instrumental in helping me with technical questions and advice through countless phone calls and visits to the AFIT facility.

Finally, I owe all of the glory to God and his son Jesus Christ. He is my guiding light and my strength.

Stephen J. Koether

Table of Contents

Page

Abstract iv

Acknowledgements v

Table of Contents vi

List of Figures viii

List of Tables x

List of Symbols xi

List of Abbreviations xii

I. .....Introduction 1
- 1.1 Research and Design Perspective 1
- 1.2 Ultra Compact Combustor Concept 2
- 1.3 Objectives 4
- 1.4 Methods 5

II. .....Theory and Background 7
- 2.1 UCC Research 7
  - *Traditional Combustor Design* 7
  - *Trapped Vortex Combustion* 8
  - *Centrifugally Enhanced Combustion* 9
  - *Inter-Turbine Burning* 10
  - *Current Experimental Research on the UCC* 11
- 2.2 Laser-Induced Fluorescence 13
  - *Mechanics of LIF* 14
  - *Detection of the OH Radical* 16
  - *Quenching* 16

III. .....Methodology 17
- 3.1 System Operation 17
  - *Combustor Rig Air and Heaters* 18
  - *Fuel Supply* 21
  - *Emissions Collection* 22
  - *Rig Installation* 24
  - *Exhaust System* 25
- 3.2 Laser Diagnostic System 26
  - *Beam Path* 28
  - *Measuring Wavelength and Power* 31
  - *LIFBASE* 32
  - *Camera* 34
  - *Hencken Burner* 35

Page

Mass Flow Controllers 37
Theoretical Equilibrium Data 40
Quenching 41

IV. .....Results and Discussion 44
4.1 Facility Validation 44
4.2 LIF Results 47
Results of basic setup for OH LIF 48
Intensity variation as a function of length 55
System uncertainty 58
Concentration Data 59
Flame Temperature 63
Spatial Data 67

V.....Conclusions 69
5.1 Overview of Project 69
5.2 Future Work and Recommendations 70

Appendix A: Mass Flow Tables for the Main Air Line 72

Appendix B: Mass Flow Tables for Secondary Air Line 73

Appendix C: Bundle Diagram 74

Appendix D: STANJAN Data for Hydrogen-Air Flame 75

Appendix E: Laboratory Start-Up and Shutdown Procedures 76

Appendix F: Laser and Camera Start-up and Shutdown Procedure 80

References 82

List of Figures

Page

Fig. 1. UCC cross section (Ref. 2) 3
Fig. 2. Detail of the UCC (Ref. 3) 4
Fig. 3. Traditional combustion chamber (Ref. 7) 7
Fig. 4. Trapped vortex combustion (Ref. 3) 8
Fig. 5. Typical engine cycle (dashed line) and a CT engine cycle (solid line) (Ref. 1). 10
Fig. 6. a) Depiction of fluorescent absorption and emission. B) Emission spectra (Ref. 19) 14
Fig. 7. Computer control station 17
Fig. 8. Rig airlines 18
Fig. 9. Main and secondary PID output displays 19
Fig. 10. Gaumer electric heaters 20
Fig. 11. Gaumer electric heater circuit breaker 21
Fig. 12. ISCO fuel pump 21
Fig. 13. Mokon heat transfer fluid pump and heater 23
Fig. 14. Infinite radius ultra compact combustor 24
Fig. 15. Combustor and surrounding parts 25
Fig. 16. Exhaust system 26
Fig. 17. Schematic of laser diagnostic setup for OH PLIF 27
Fig. 18. Pictorial schematic of the laser system 28
Fig. 19. Laser control station 28
Fig. 20. Bosch support structure 29
Fig. 21. Beam path part 1. 29
Fig. 22. Beam path part 2 30
Fig. 23. Wavelength meter 31
Fig. 24. LIFBASE input screen 32
Fig. 25. LIFBASE absorption spectral simulation for OH at 1800K 33
Fig. 26. Princeton Instruments ICCD camera 34
Fig. 27. Camera control station 35

Page

Fig. 28. Hencken burner 36
Fig. 29. Schematic of Hencken flame and beam interaction 37
Fig. 30. MKS ALTA digital mass flow controllers 37
Fig. 31. MKS 247D Four Channel Power Supply/Readout 38
Fig. 32. BIOS Definer 220H Flow Meter 38
Fig. 33. Mass flow meter calibration data 39
Fig. 34. Main vane temperature profile 44
Fig. 35. Cavity temperature profile 45
Fig. 36. Pressure profile for heated air experiment 46
Fig. 37. Equilibrium temperature of a hydrogen-air flame 48
Fig. 38. Full range of OH absorption at 2400 K from 240 nm to 400 nm 49
Fig. 39. Temperature dependence of various LIFBASE lines. Provided by Meyer (Ref. 24). 50
Fig. 40. OH emission spectra at T = 2300 K 51
Fig. 41. Excitation and detection process summary 52
Fig. 42. Image dimensions with the interaction of the Hencken flame and laser sheet 53
Fig. 43. Actual camera image 54
Fig. 44. Typical averaged image minus the background 55
Fig. 45. Intensity variation in the x-direction through the center of the laser sheet 56
Fig. 46. Intensity variation in the y-direction through the center of the flame 57
Fig. 47. Schematic of analysis area for all images 57
Fig. 48. Average intensity for 50 images at an equivalence ratio of 1.0 58
Fig. 49. Theoretical OH concentration from STANJAN 59
Fig. 50. Experimental intensity and theoretical OH concentration 60
Fig. 51. Quenching corrected experimental data and theoretical OH concentration 62
Fig. 52. LIFBASE simulation at T = 2500 K 64
Fig. 53. LIFBASE simulation at T = 1800 K 64
Fig. 54 Theoretical and experimental flame temperature 66
Fig. 55. Spatial profile for the Hencken flame 67
Fig. 56. Bundle diagram 74

List of Tables

Page

Table 1. Range of electronic transition for selected molecules (Ref. 20) 15

Table 2. STANJAN inputs for hydrogen-air flame 41

Table 3. Quenching rate parameters from Tamura et al.(Ref. 22) 42

Table 4. OH LIF efficiencies for a hydrogen-air flame 61

Table 5. Percent error between theoretical concentration and uncorrected and quenching corrected intensity 62

Table 6. LIFBASE ratios of peak magnitudes 65

Table 7. Experimental flame temperatures 66

Table 8. Mass flow rates for the main air line 72

Table 9. Mass flow rates for the secondary air line 73

Table 10. Mole fractions of products in a hydrogen-air flame 75

Table 11. PPM of products in a hydrogen-air flame 75

List of Symbols

Symbol	
A	Einstein A Coefficient (s^{-1})
$\mathring{A}$	Angstrom (1×10^{-10} meters)
C_2	Diatomic carbon
CH_4	Methane
CO	Carbon Monoxide
CO_2	Carbon Dioxide
C_2H_2	Acetylene
C_2H_4	Ethylene
g	Gravitational constant (m/s^2)
H_2O	Water
k	Boltzmann's Constant $\left(\frac{m^2 kg}{s^2 K}\right)$
M	Molecular Mass (kg/kmol)
N_2	Nitrogen
NO	Nitric Oxide
NO_X	Oxides of Nitrogen
NO_2	Nitrogen Dioxide
OH	Hydroxide
O_2	Oxygen
Q	Quinching Rate (s^{-1})
S_B	Buoyant flame speed (m/s)
ϕ	Equivalence Ratio
σ	molecule cross section $\left(\mathring{A}^2\right)$

List of Abbreviations

Abbreviation	
AFIT	Air Force Institute of Technology
AFRL	Air Force Research Laboratory
CAI	California Analytical Insturments
CARS	Coherent Anti-Stokes Raman Spectroscopy
CCD	Charge coupled device
CFD	Computational Fluid Dynamics
FCU	Frequency Conversion Unit
FDU	Frequency Doubling Unit
ICCD	Intensifying Charge Couple Device
IGV	Inlet guide vanes
ISSI	Innovative Scientific Solutions Inc.
ITB	Inter-stage turbine burner
LDV	Laser Doppler Velocimetry
LID	Low image density
LIF	Laser-Induced Fluorescence
LII	Laser-Induced Incandescence
LSV	Laser speckle Velocimetry
mA	milli-Amps
mJ	milli-Joule
Nd:YAG	Neodymium-doped yttrium aluminum garnet
nm	nanometer
PID	Proportional-integral-derivative
PIV	Particle Imaging Velocimetry
PLIF	Planar Laser Induced Fluorescence
ppm	Parts per million
PRV	Pressure reducing valve
RVC	Radial Vane Cavity
SAE	Society of Automotive Engineers

SCFM	Standard cubic feet per minute
SCXI	Signal Conditioning Extension for Instrumentation
SLPM	Standard Liter Per Minute
ST	Specific thrust
TSFC	Thrust specific fuel consumption
TVC	Trapped Vortex Combustion
UCC	Ultra Compact Combustor
VI	Virtual Instrument
2-D	Two dimensional
3-D	Three dimensional

VALIDATION OF THE AFIT SMALL SCALE COMBUSTION FACILITY AND OH LASER-INDUCED FLUORESCENCE OF AN ATMOSPHERIC LAMINAR PREMIXED FLAME

I. Introduction

1.1 Research and Design Perspective

The rising cost of energy has opened the door for continued research to make Department of Defense operations more efficient. This is especially true in the sense of air operations since the United States Air Force is one of the largest petroleum consumers in the country. The Global War on Terror and other threats throughout the world dictate the demand for air operations will not decrease in the near future. The bottom line from an aircraft propulsion perspective, is the slightest improvements in turbine engine efficiency can equate to millions of dollars saved by the US Air Force and Department of Defense.

The Ultra-Compact Combustor (UCC) is one of the many areas being studied as a solution to make gas turbine engines more efficient. The UCC burns air and fuel in a swirling manner to significantly reduce the axial length needed for combustion. The UCC is being studied for two possibilities, first as an inter-stage turbine burner (ITB) to improve thermodynamic efficiency through a re-heat cycle in the turbine section. Secondly, the UCC could potentially be used as the primary combustor between the compressor and turbine resulting in a major reduction in weight without a loss in thrust. Previous experiments have proved the UCC is a viable and promising concept. However, little is known about the flow field within the UCC due primarily to geometry constraints and not being able to see inside the combustor.

The newest method in combustion diagnostics is laser spectroscopy because of its non-intrusive nature and ability to produce real time results. A new facility at the Air Force Institute of Technology (AFIT) has been built for the sole purpose of combustion diagnostics starting with the study of a sectional model of the full UCC. A sectional model is used to overcome the geometry constraints of the full-scale model. This facility will also provide future combustion related testing capabilities for future AFIT experiments.

1.2 Ultra Compact Combustor Concept

The Ultra-Compact Combustor was developed by the US Air Force Research Laboratory (AFRL), Propulsion Directorate at Wright-Patterson Air Force Base in Dayton, Ohio. The concept of the UCC was inspired by the idea of a constant temperature (CT) cycle gas turbine engine proposed by Sirignano and Liu (Ref. 1). A CT cycle can produce large gains in specific thrust (ST) with the same or reduced thrust specific fuel consumption (TSFC). The problem is that a true CT cycle is virtually impossible because it requires burning inside the turbine rotor. The most practical alternative to achieving a similar effect is an inter-stage turbine burner (ITB). Since traditional combustors are much too large to fit between turbine stages, the concept of the UCC was born.

The overall goal of the Ultra-Compact Combustor is to greatly reduce the size of traditional gas turbine combustion devices. Combustion in the UCC occurs in a cavity that wraps around the circumference of the engine as shown in Fig. 1.

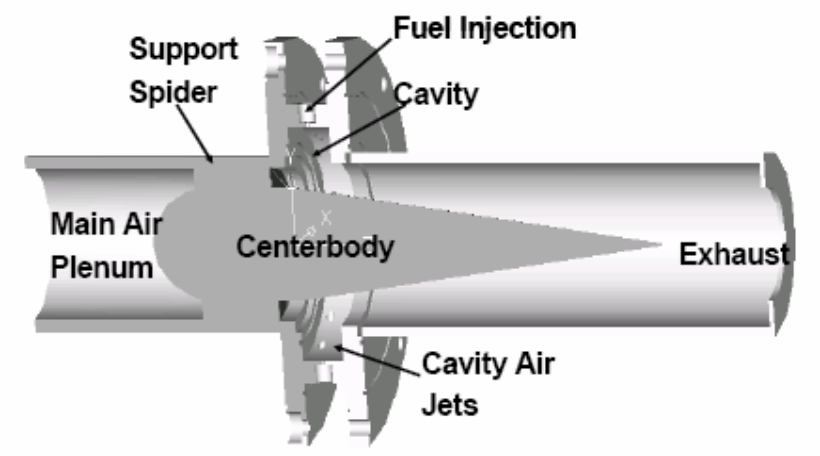

Fig. 1. UCC cross section (Ref. 2)

Air is injected into the cavity through angled inlets to create a highly swirled flow while fuel is injected into the cavity through recessed ports. Flame stability is achieved through trapped vortex combustion (TVC). The swirling fuel and air inside the cavity create a high g-load on the mixture that increases the flame speed and reduces the chemical time required for combustion (Ref. 2). The cavity is open to the main axial flow through the combustor. Airfoils on the centerbody in Fig. 1 simulate inlet guide vanes (IGV) or stator blades. In each airfoil, there is a radial vane cavity (RVC) establishing an intermediate combustion zone and helps draw the mass from the cavity into the main flow by creating a pressure gradient. The guide vanes and RVCs can be seen in Fig. 2.

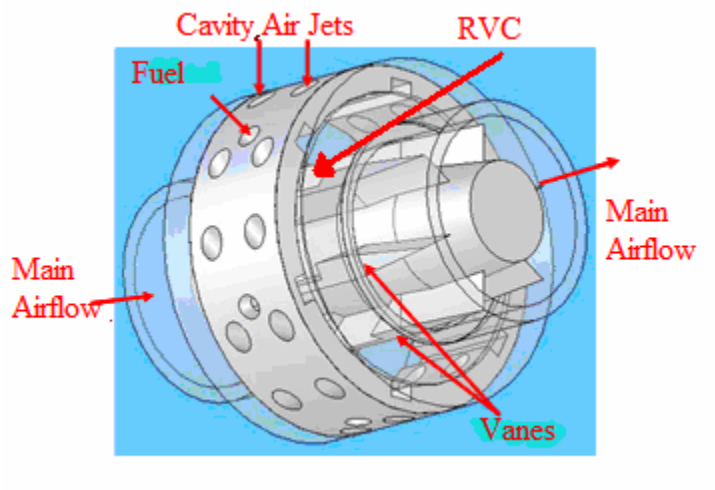

Fig. 2. Detail of the UCC (Ref. 3)

1.3 Objectives

Construction of the AFIT combustion facility began in 2005 with Dittman (Ref. 4). Dittman (Ref. 4) succeeded in purchasing and setting up most of the major hardware components in the lab. Anderson (Ref. 5) followed on in mid 2006. At the completion of Anderson's work, a LabView Virtural Interface (VI) that runs the entire lab was complete and most of the hardware components had been wired and connected. Anderson (Ref. 5) succeeded in creating a centralized computer control and data acquisition station for the combustion lab. Although most of the hardware was in place when Anderson was complete, the facility lacked validation of the various components. In other words, most of the hardware had not been turned on, tested or controlled.

The AFIT combustion lab is not the only Air Force laboratory researching the UCC and other combustion devices. However, the capabilities of the new laser diagnostic system set the AFIT combustion lab apart. At the beginning of this phase of the project, the components of the laser system had been delivered but had not been set up or

configured. The laser system is capable of several diagnostic techniques including Laser-induced Fluorescence (LIF), instantaneous Raman, Particle Image Velocimetry (PIV), Laser-induced Incandescence (LII), Coherent Anti-Stokes Raman Scattering (CARS), and Raman Spectroscopy. The first technique to be used in the AFIT combustion lab is the Laser-induced Fluorescence (LIF).

The objective is to get the AFIT lab fully functional and ready to test the sectional UCC rig. This includes validating the hardware components in the lab, setting up the laser system for LIF, and calibrating the laser system.

1.4 Methods

To meet the objective of a fully operational lab, the steps taken were:

1. *Validating the major components of the lab.* This includes turning on and controlling the major components already in the lab. Every system supporting the combustion process must be tested to ensure safety and reliability.
2. *Making necessary corrections to each system.* Inevitably when turning equipment on for the first time problems will ensue. This means re-designing and coming up with creative solutions to overcome problems that arise. This also includes making the necessary purchases for lab completion.
3. *Establishing operational procedure.* It is vital to come up with step-by-step operational procedure for the lab. Accurate procedures will ensure safety in a potentially dangerous environment and will also ensure continuity in experimental results.
4. *Get the facility certified for combustion experiments.* Once the major systems have been validated, only then can the lab be certified through official channels.

This includes the WPAFB Fire Marshal, AFIT Safety, Health and Bio, and the Environmental office. This also means implementing the changes that those officials require.

5. *Setting up and configuring the laser system.* The laser system is the focal point of the lab. To get the system setup, the lasers must be aligned and optics must be set. The systems must be configured for LIF since it is the first diagnostic technique to be used.
6. *Calibrating the laser system.* Before applying the LIF techniques to an unknown combustion environment it is imperative to test and calibrate the system to ensure it is working properly.

II. Theory and Background

2.1 UCC Research

Traditional Combustor Design

In traditional gas turbine combustors, the air enters the combustor from the compressor and fuel is injected axially into the flow. This type of design is often referred to as combustion can or flame tube. Combustion in these types of devices occurs in two zones. First is a primary zone where the fuel and air mix and begin to combust. This zone is typically characterized by stoichiometric or slightly fuel rich combustion. When the air enters the combustor, it is directed around the fuel injector which causes recirculation. This recirculation around the fuel injector is what causes the combustor to stay lit (Ref. 6).

The flow then enters a secondary or dilution zone where air is added and the mixture becomes fuel lean. The addition of air lowers the temperature of the gas to prevent damage to the high-pressure turbine (Ref. 7). Fig. 3 shows a schematic of a typical combustion chamber.

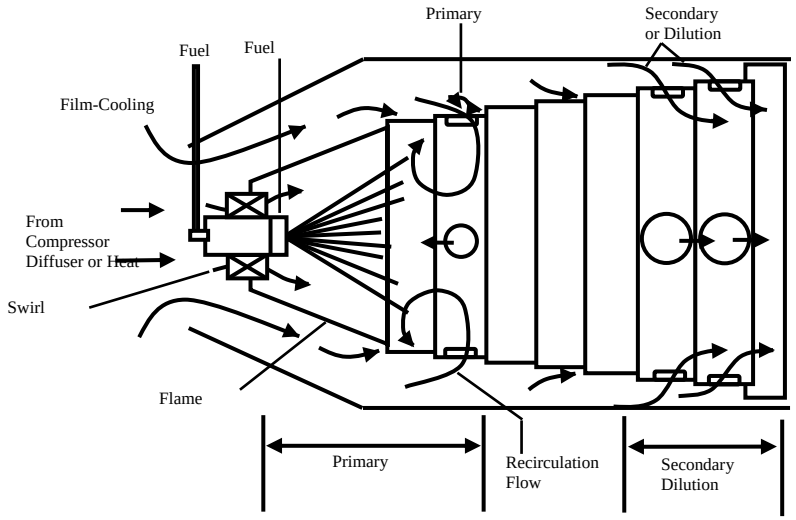

Fig. 3. Traditional combustion chamber (Ref. 7)

Although the UCC operates under different circumstances, it still incorporates the same principles of the combustion zones as traditional combustors. The circumferential cavity acts as the primary zone and the cavities in each radial vane act as the secondary zone (Ref. 8).

Since combustion in traditional devices happens axially, the length of the combustor is governed by the residence time. The axial combustion also causes significant losses because the flow often must slow down for combustion to occur.

Trapped Vortex Combustion

One of the major concepts leading to the development of the UCC is trapped vortex combustion (TVC). In this concept, a vortex is created by axial flow passing a recessed cavity. Air and fuel is then added in the same direction as the vortex in order to strengthen it. Once lit, the vortex actually stabilizes the flame. The TVC concept is shown in Fig. 4.

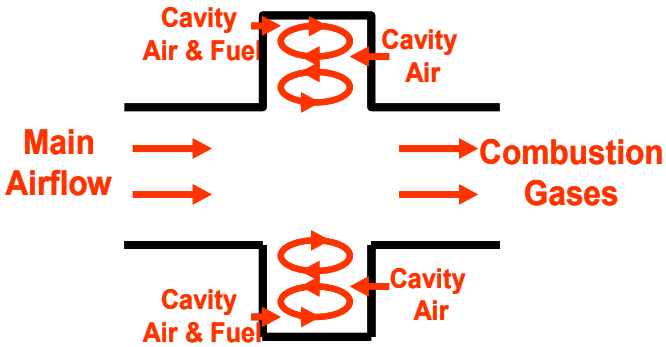

Fig. 4. Trapped vortex combustion (Ref. 3)

The first designs of a TVC showed the recessed cavity essentially acted as a shielded pilot flame that produced a constant ignition source and improved lean-blow-out (Ref. 9).

The TVC design allows for higher velocities outside the cavity that leads to improved combustion efficiency (Ref. 9).

The UCC uses a trapped vortex to improve mixing of fuel and air and aid in flame stabilization. The other concept the UCC incorporates is that of centrifugally loaded swirling.

Centrifugally Enhanced Combustion

Centrifugal forces on a combustion mixture can greatly increase the flame speed because buoyancy effects help transport the flame into less dense regions (Ref. 10). Lewis (Ref. 10) is accredited with pioneering the research that led to this conclusion. The buoyant force on a particle is calculated by the following equation (Ref. 10):

$$F_B = \rho_a g \left[1 - \frac{\rho_f}{\rho_a} \right] \tag{1}$$

Typically, this buoyant force is very small for hot gases and laminar and turbulent flame speeds are dominant in spreading the flame. However when the combustion is centrifugally loaded, the magnitude of gravitational acceleration, g, in Eq. 1 drastically increases and in turn the buoyant force becomes very large. In fact, the buoyant force becomes so that buoyancy effects spread the flame much faster than typical laminar or turbulent flame speeds. Lewis (Ref. 11) found below 200 g the buoyant force has little effect on combustion, between 200 g and 500 g the buoyancy effects start to become dominant, and above 500 g the buoyancy flame speed (S_B) is dominant and can be found by (Ref. 10):

$$S_B = 1.25\sqrt{g} \tag{2}$$

Lewis (Ref. 11) also found the flame speed would peak at a loading of around 3500 g and then begin to decrease.

This concept was studied further by Yonezawa et al. (Ref. 12) in a jet swirled combustor. They determined that increases in efficiency could be obtained with high centrifugal loading.

The two major principles for the UCC are trapped vortex and centrifugally loaded combustion. The trapped vortex mixes and stabilizes the flame while centrifugal loading increases the flame speeds to allow combustion to occur in a very small area.

Inter-Turbine Burning

Currently, most UCC research is geared toward the development of an inter-turbine burner (ITB). As previously mentioned, Sirignano and Liu (Ref. 1) proposed the idea of a constant temperature (CT) gas turbine engine. They showed constant temperatures through the turbine stages could greatly improve the performance of the engine. A typical engine cycle for a gas turbine engine is represented by a dashed line in Fig. 5, while the proposed constant temperature cycle is represented by a solid line.

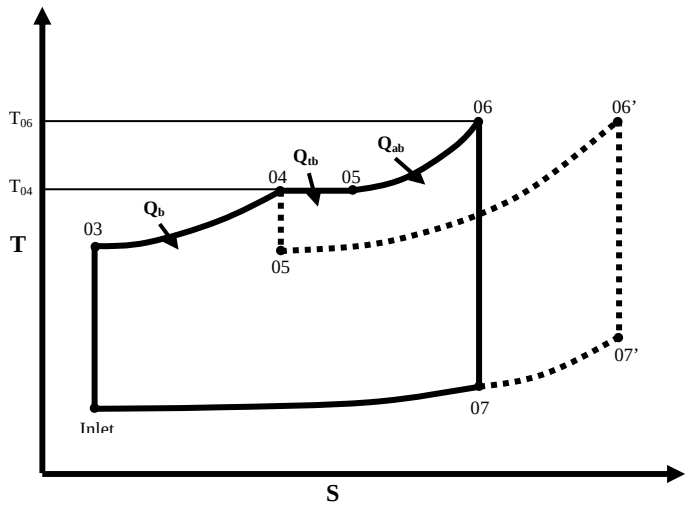

Fig. 5. Typical engine cycle (dashed line) and a CT engine cycle (solid line) (Ref. 1).

Using a constant temperature model, Sirignano and Liu (Ref. 1) predicted an improvement in specific thrust of over 50% with little impact on thrust specific fuel consumption. To actually implement a CT cycle burning in the rotor stage would have to be implemented which is much too difficult.

The most viable alternative to this is an inter-turbine burner (ITB). Ideally, an ITB would burn in the stator sections of the turbine. The problem is that traditional combustors are much too large and will not fit between turbine stages. Thus, the UCC using trapped vortex and centrifugally loaded combustion provides a solution to this problem. Using the UCC as an ITB could increase cycle efficiency with only minor increases in weight.

Current Experimental Research on the UCC

The Air Force Research Labs (AFRL) began experiments on the UCC in 2001. Anthenien et al. (Ref. 13) performed the first studies on a UCC by varying equivalence ratios of air and JP-8 over a wide range of operating conditions at atmospheric pressure. The results of the experiment were promising. Much shorter wavelengths were observed as compared to a swirl-stabilized combustor, lean blowout was near an equivalence ratio of $\phi = 0.5$, and efficiencies of greater than 99% were achieved up to an equivalence ratio of $\phi = 2.0$ (Ref. 13).

In 2003, Zelina et al. (Ref. 14) found the angle and type of fuel injector used in the UCC had a large impact on combustion efficiency. For low centrifugal loadings, Zelina et al. (Ref. 14) found the flame was injector-stabilized and at high centrifugal loadings the flame was bulk-flow stabilized. They also found the combustion chamber

had a small pressure drop of 2% and a high g loading created high radial turbulence in the cavity that increased combustion efficiency (Ref. 14).

Also in 2003, UCC experiments using a Laser Doppler Velocimeter (LDV) found circumferential velocities of 20-45 m/s with accelerations of 1000 to 4000 g within the cavity (Ref. 15). The results by Quaale et al. (Ref. 15) also showed the cavity velocities were relatively insensitive to main flow velocity and confirmed that an increase in g-loading means an increase in combustion efficiency.

More recently, the UCC has been tested in a high-pressure environment. The high-pressure tests show the UCC should operate at 97 to 99% combustion efficiency over a wide range of operating conditions in a high-pressure environment (Ref. 16). The major tests still ongoing for the UCC at AFRL include increasing efficiency, reducing lean blowout, and reducing emissions in all pertinent environments.

Currently, the experimental results for the UCC are promising. However, there are still questions about the physics of the flow inside of the cavity and how the cavity flow interacts with the guide vanes and RCV. This has not been studied by AFRL primarily due to the geometry constraints of the full-scale UCC rig. In response, a 2-D sectional rig has been designed to allow greater optical access to study the flow fields and combustion within the UCC. To help design the rig a computational fluid dynamic (CFD) model was created by Moenter (Ref. 17). Moenter started the design of both a flat and curved sectional cavity. Once Moenter (Ref. 17) created the CFD code, the CFD results were matched to the experimental results of the full UCC at AFRL. The final flat section, also referred to as the infinite radius section, was completed by Anderson (Ref. 5) and construction on that model is now complete.

2.2 Laser-Induced Fluorescence

Traditionally, combustion diagnostics is primarily done in a two ways. The most common method is sampling. In this method, a sample of the combustible gas is gathered followed by some sort of analysis on the sample. There are a couple of problems with this, first the combustion process occurs through a series of chemical reactions and just because the sample may be taken out of the process, the molecules in the sample will not stop reacting with one another. In other words, it is hard to get really time accurate results because by the time analysis on the sample has been completed the composition of the sample can be completely different than when it was first gathered. Another problem is that for any kind of reliability the sample has to be very carefully controlled, which usually means keeping the sample at a precise temperature.

Another commonly used method is probing. Probing involves putting some solid object or probe into the flame. Often the probe is a thermocouple or some other temperature measuring device. The problem is that a probe is intrusive to the flame. In other words, it disrupts the flame and changes the dynamics of combustion resulting in inaccurate data about the true nature of the flame.

Accurate combustion diagnostics are possible with the use of laser spectroscopic methods. The benefit of laser spectroscopic techniques is that they give instant, real time information about the flame and combustion process (Ref. 18). The other big advantage to using laser spectroscopic methods is they are non-intrusive and do not disrupt the flame. Moreover, the methods are accurate and provide high resolution.

One particular laser spectroscopic method is Laser- Induced Fluorescence (LIF). LIF is a two-dimensional imaging technique widely used in combustion diagnostics.

From a combustion standpoint, LIF is most commonly used to calculate the concentrations of different species and the temperature within a flame.

Mechanics of LIF

The concept of fluorescence is relatively simple. Fluorescence is simply an energy absorption followed by a light emission (Ref. 18). In the case of LIF, a photon is generated by a laser that excites a molecule to a higher energy state, but the molecule does not like to stay at that excited state. So in order for the molecule to return to a lower energy state, it then emits light at the same and different wavelengths. The light that is emitted by the molecule make up the fluorescent signal and is generally detected by a camera to produce in an image. The fluorescence signal or intensity directly correlates with the concentration of the emitting species (Ref. 18). The stronger the fluorescent signal the higher the concentration of the species. The fluorescence phenomenon is depicted in Fig. 6a by an arrow going up representing the photon being absorbed and moving to a higher energy state, and then an arrow going back down representing a photon release and return to a lower energy level. For LIF, the absorption occurs at a precise wavelength and the emission occurs over a span of different wavelengths which is depicted in Fig. 6b.

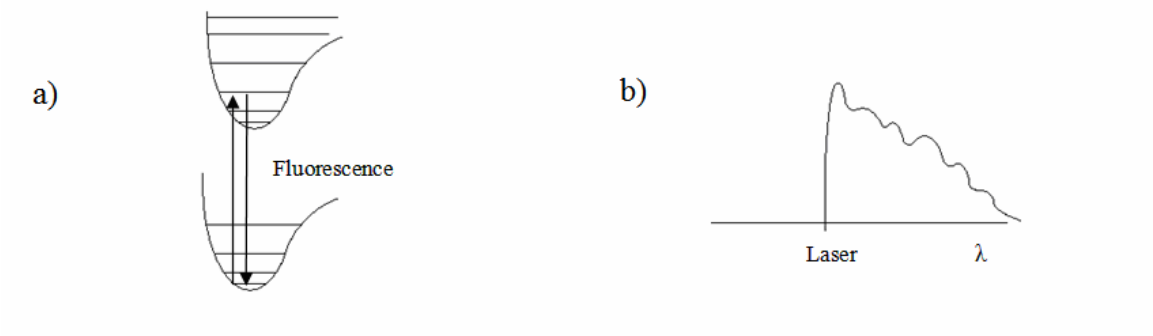

Fig. 6. a) Depiction of fluorescent absorption and emission. B) Emission spectra (Ref. 19)

LIF can be used to detect the concentration of several different molecules in a combustion environment. Most electronic transition occurs within the visible light spectrum and almost all important molecules in a combustion environment containing H, O, C, N, and S have been detected by LIF (Ref. 18). However, every molecule has its own discrete region of spectral absorption. This means each molecule will only absorb a photon at very specific wavelength. Table 1 shows a list of common species detected using LIF methods and the known range of electronic transition for that molecule.

Table 1. Range of electronic transition for selected molecules (Ref. 20)

Molecule	Electronic Transition (nm)
C_2	400-600
	230-330
CH radical	500-430
	450-360
CO	200-250
	150-240
N_2	100-500
	Vac u.v.
NO	195-340
	200-500
O_2	500-900
	170-220
OH radical	240-400
CH_4	145.5-500
C_2H_2	237-210
CO_2	140-170
H_2O	145-186

Table 1 should really only be used as a guide, because electronic transition does not occur over the entire range listed, but rather at a few discrete wavelengths within that range. Therefore, a prerequisite of any LIF experiment is a database of known absorption spectra for the molecule of interest. One such database is LIFBASE which will be discussed in further detail later (Ref. 21).

Detection of the OH Radical

The most common molecule detected by LIF methods in combustion research is the OH radical. The OH molecule is good for combustion diagnostics because it is a radical that is produced in the intermediate reactions of combustion and then destroyed by the end of the combustion process. The OH radical is very abundant in most flames and its spectroscopy is well known (Ref. 18). The OH molecule is a great indicator of the behavior of the flame and can provide information on flame mixing, propagation, ignition, structure, and local extinction (Ref. 18). Since OH is a good indicator of flame fronts, it is good for calculating the temperature of the flame. In general, a higher concentration of OH will lead to a higher temperature.

Quenching

The fluorescent quantum yield is the most important quantity when trying to determine concentration and temperature from fluorescent signal (Ref. 18). The fluorescent signal strength is adversely affected by quenching. Essentially, quenching is the depopulation of the excited energy state without releasing a fluorescent signal. Quenching depends mostly on the cross section and quantity of the other molecules in the mixture. The cross sections of the species in the mixture is dependent on the temperature of the flame (Ref. 22). Analytical models, such as the one published by Tamura et. al (Ref. 22), must be used to adjust the LIF signal for quenching effects. The quenching effects are the biggest disadvantage to using LIF methods because the information available for the analytical models used to correct the LIF is somewhat limited (Ref. 5).

III. Methodology

3.1 System Operation

The laboratory is divided into two systems, first is the computer and hardware associated with the functionality of the combustion device. The centerpiece for this system is the main computer in Fig. 7 with the LabView software that make up the command and control center for the lab. The computer provides the ability to control the major elements in the lab remotely, as well as providing data acquisition for monitoring various inputs and outputs of the experiment.

Fig. 7. Computer control station

The computer control and data acquisition for the major hardware systems in the lab is covered in detail by Anderson (Ref. 5) and will not be covered again here. Instead, only the significant changes and advances to the major components will be discussed.

Combustor Rig Air and Heaters

Two Ingersoll-Rand compressors in building 644 provide air for use in the laboratory. The air comes into the room at approximately 10.3 bar (150 psig) in a single 38.1 mm (1.5 in) copper pipe. Once in the room, it is split (on the far right side of Fig. 8) into a main airline that is capable of delivering up to 7 kg/min (200 SCFM) and a secondary line that is capable of delivering up to 2 kg/min (60 SCFM) (Ref. 5).

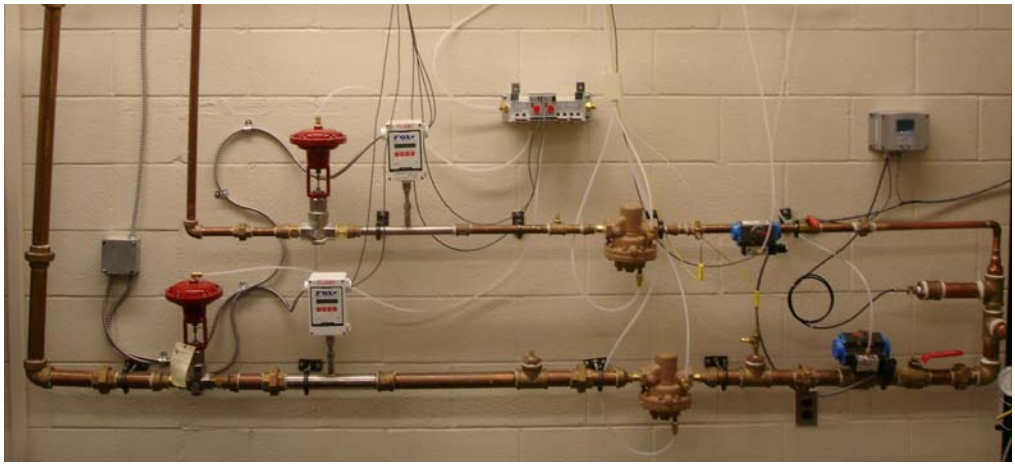

Fig. 8. Rig airlines

Starting from the right side of Fig. 8, the air in each line goes through a manual ball valve and then a blue and grey UCI pneumatically actuated ball valve. The air then passes through a Dwyer 682-0 pressure transducer, a K-type thermocouple and a manually operated CASHCO pressure-reducing valve (PRV). This PRV is controlled by a knob on the computer control station. Following the manual PRV is a Fox Instruments FT2 thermal mass flow meter that transmits flow rate and temperature to the computer. Downstream of the Fox flow meter is a Badger Meter pneumatically actuated needle valve that provide precise control of the airflow. The mass flow rate is then transmitted to two GC Controls 2404 PID controller mounted on the computer control station shown in Fig. 9.

Fig. 9. Main and secondary PID output displays

At the beginning of this phase of the project, all of the above mentioned hardware was in the lab. However, the air had not yet been turned on or controlled. Each component in the air line was tested starting with the UCI pneumatic ball valve and proceeding down stream. The majority of the work added was configuring the Proportional-Integral-Derivative (PID) controllers. The PID controllers were initially configured using the auto-tune mode but it resulted in an unsteady airflow. Instead, each controller was manually configured by changing integral and derivative times through trial and error until the controllers kept the mass flow of the air constant. The PID controllers display a percentage and Appendix A and Appendix B contain conversion tables for a quick reference between percentages and flow rates in both SI and English units for the main and secondary lines. The manufacturing specifications on all the devices associated with the rig air lines accompanied with wiring diagrams can be found in Anderson (Ref. 5).

Once the air leaves their respective Badger Meter needle valve it passes through a Gaumer electric heater on the way to the combustor stand. Fig. 10 shows the heaters for both the main and secondary lines.

Fig. 10. Gaumer electric heaters

The main line passes through a 37.5 kW heater and the secondary line passes through a 12.3 kW heater, both lines have a maximum outlet temperature of 538 °C (1000 °F). At the beginning of this phase of the project, the heaters were installed and the airlines were connected. The heaters were turned on for the first time but were unable to be controlled from the central computer. This resulted in numerous calls to the manufacturer to reconfigure the heaters to send and receive a 4-20 mA signal. The heaters now work properly and are able to be controlled from the main computer system. Power to the heaters runs through a breaker box shown in Fig. 11. The breaker in Fig. 11 must be turned on before being able to control it from the computer.

Fig. 11. Gaumer electric heater circuit breaker

Fuel Supply

Two ISCO 1000D syringe pumps (shown in Fig. 12) provide the combustor with a constant supply of fuel. The fuel pump is capable of providing 5.67 mL/s at 137.9 bar with an accuracy of 25.38 nL (Ref. 4).

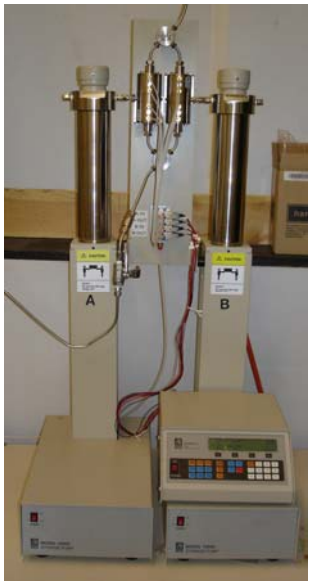

Fig. 12. ISCO fuel pump

The fuel used in the UCC is JP-8 jet fuel. The main contributions to the fuel system were tracking down and acquiring JP-8 for use in the lab. The fuel is located in a flame proof cabinent and is connected to the pumps via 6.35 mm (¼ in) stainless steel tubing. The fuel pumps are controlled by the computer control station.

Emissions Collection

A California Analytical Instruments (CAI) Raw Emissions Test Bench is used to analyze combustor emissions. This test bench is capable of accurately detecting total hydrocarbons (THC), carbon dioxides (CO_2), carbon monoxide (CO), oxygen (O_2), and nitrous oxides (NOx) (Ref. 5). The detection of the gases by the CAI meets the specifications for raw emissions as defined in SAE ARP 1256 (Ref. 4).

To protect the CAI test bench and obtain accurate data, the emission sample from the combustor must be maintained at a temperature of 433 K ± 15 K (Ref. 4). The sample is collected by a stainless steel exhaust probe. Inside the exhaust probe is a cross flow heat exchanger that uses Duratherm Heat Transfer Fluid to maintain the probe at a constant 433 K. The oil acts a coolant because the hot exhaust leaving the combustor has the potential to overheat and melt the exhaust probe. The Duratherm Heat Transfer Fluid is heated and circulated by a Mokon H22103AJ Compact Heated Thermal Fluid System shown in Fig. 13.

Fig. 13. Mokon heat transfer fluid pump and heater

Once the sample leaves the emission probe it travels through 6.35 mm (¼ in) flexible, braided Teflon tubing through two stainless UCI 3-way valves. The UCI valves are also connected to an incoming nitrogen (N_2) line that is used to purge the emissions lines once testing is complete. The emissions sample continues through 6.35 mm (¼ in) flexible, braided Teflon tubing until it reaches a Unique Products International heated gas filter and 9 m (30 ft) heated line. All braided Teflon tubing is heated by Watlow electronic tube heaters to maintain the sample at 433 K. The heated 9 m (30ft) line takes the sample all the way to the CAI emissions test bench.

The contributions to the emission collection first include cleaning and priming the Mokon Thermal Fluid System. The system was tested and operating procedures have

been established for the Mokon machine. Secondly, the Watlow tube heaters and heating tape were properly wired. Finally, a 120 volt outlet was wired to the combustion stand for power supply to the Watlow heaters and heating tape.

All gases for the lab and the CAI test bench come in from the tank farm via two bundles of seven 6.35 mm (¼ in) copper tubing. The diagram and labeling for each bundle and location in the tank farm can be found in Appendix C.

Rig Installation

The infinite radius ultra compact combustor, shown in Fig. 14, is installed on an 80/20 extruded aluminum stand. All work for the UCC installation was all done after Anderson (Ref. 5). The red arrows in Fig. 14 indicate the direction of airflow.

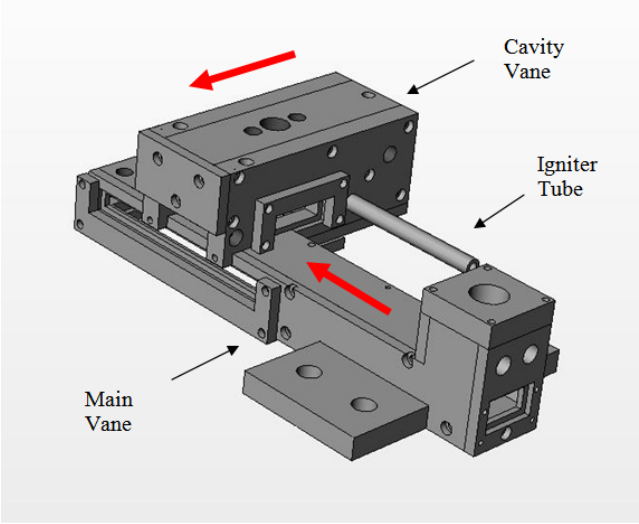

Fig. 14. Infinite radius ultra compact combustor

The stand not only provides a mount for the combustor, but also for all incoming fuel, gas, and instrument devices. The combustor is monitored by five K-type thermocouples and four pressure taps that all lead back to the computer control

station. Fig. 15 shows the combustor, combustor stand, as well as the various connections used to monitor the combustion.

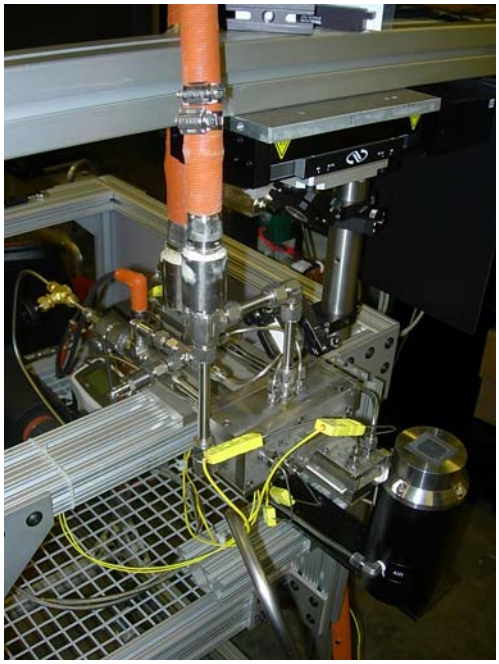

Fig. 15. Combustor and surrounding parts

The combustor stand is mounted on wheels that allow for easy adjustments for any device mounted on or around the stand.

Exhaust System

The exhaust system includes an exhaust hood and main exhaust catch shown in Fig. 16. The exhaust hood is stationed over the combustor while the exhaust catch is on a stand just off the end of the main vane exhaust.

Fig. 16. Exhaust system

The exhaust travels through 40.64 cm (16 in) diameter duct work pulled by a circular fan at approximately 1.0 kg/s (1800 SCFM) (Ref. 5). All construction and implementation of the exhaust system was done during this phase of the project after Anderson's (Ref. 5) work.

3.2 Laser Diagnostic System

The capabilities of the laser system for combustion diagnostics are what set this laboratory apart from others in the U.S. Air Force for researching the UCC. At the completion of Anderson's (Ref. 5) work, the major laser components had been delivered to the lab and the Nd:YAG laser had been initially configured. All other setup for the laser system was done during this phase of the project. The system is currently set up for

Laser-Induced Fluorescence (LIF). Fig. 17 shows a schematic of the current laser system setup for the LIF measurements.

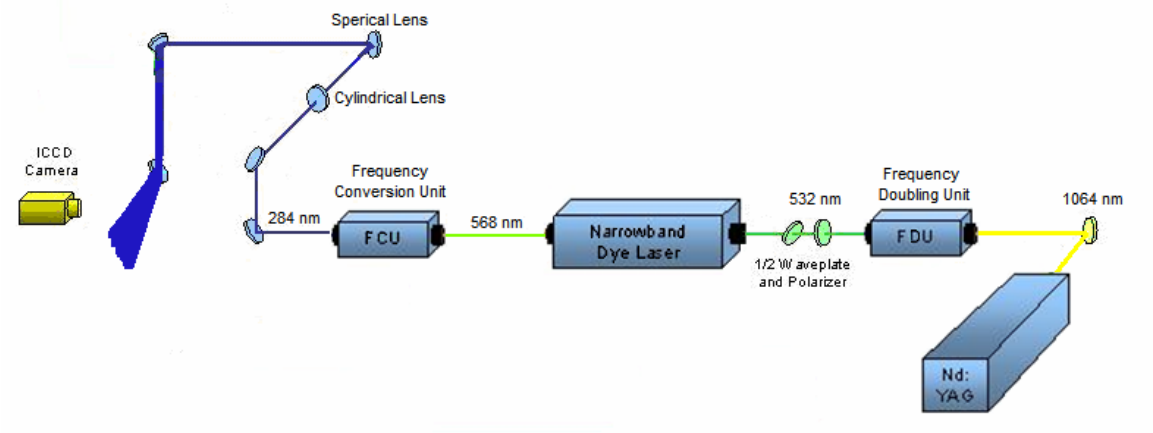

Fig. 17. Schematic of laser diagnostic setup for OH PLIF

Just as Fig. 17 shows, the laser light is generated in a Newport Spectra-Physics Quanta-Ray Pulsed Nd:YAG laser at a wavelength of 1064 nm. The beam then passes through a frequency doubling unit (FDU) where the wavelength is reduced to 532 nm before proceeding through a half waveplate and polarizer. Together the waveplate and polarizer have the ability to reduce the power of the laser before it enters the dye laser. The polarization of the beam coming out of the dye laser is vertical and the half wave plate can rotate the polarization to any desired angle up to 90°. The polarizer then allows only vertically polarized light through and rejects the rest. So for example, if it is desired to cut the power of a vertically polarized beam in half, the half waveplate would be set to an angle of 45° and the polarizer would only allow the half of the light through since only half is still in the vertical plane. Once the beam passes through the waveplate and polarizer, the beam enters a Continuum ND6000 tunable dye laser where it is tuned to the desired wavelength for the LIF experiment. The beam then travels through the frequency

conversion unit (FCU) where the frequency is again doubled. So if a wavelength of 284 nm is desired, the ND6000 dye laser must actually be tuned to a wavelength double which is why Fig. 17 shows the beam wavelength leaving the dye laser as 568. Fig. 18 is a similar schematic to that of Fig. 17 but is a pictorial schematic of the laser system.

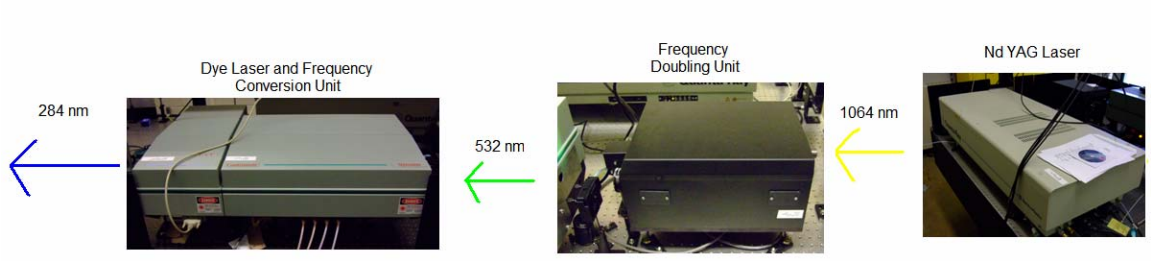

Fig. 18. Pictorial schematic of the laser system

The entire laser system is controlled by the computer and control center shown in Fig. 19 on the the large laser table. Full start-up and shutdown procedures for the entire system is located in Appendix F.

Fig. 19. Laser control station

Beam Path

Once the UV beam leaves the dye laser and frequency control unit it passes through a number of different optics that direct it toward the test subject. To support the

optics a structure between the two laser tables in the lab was constructed using Bosch 60 Series aluminum structural frame. Fig. 20 shows the final setup of the Bosch structure.

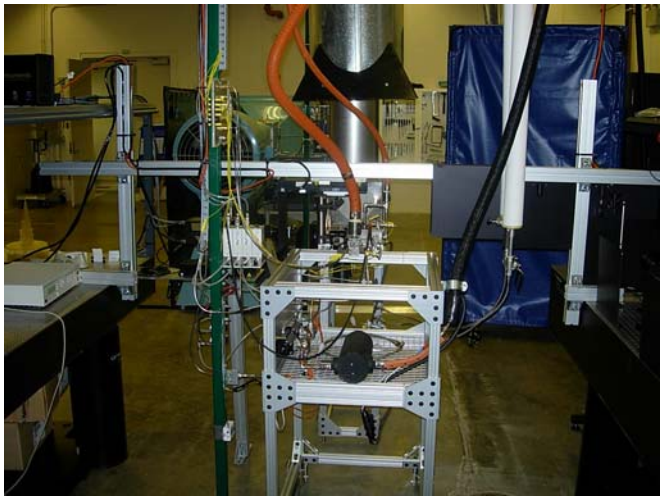

Fig. 20. Bosch support structure

Fig. 21 and Fig. 22 show the path of the laser beam once it leaves the frequency conversion unit. The path of the beam is illustrated by the blue line and every optic that it comes into contact with is numbered in red.

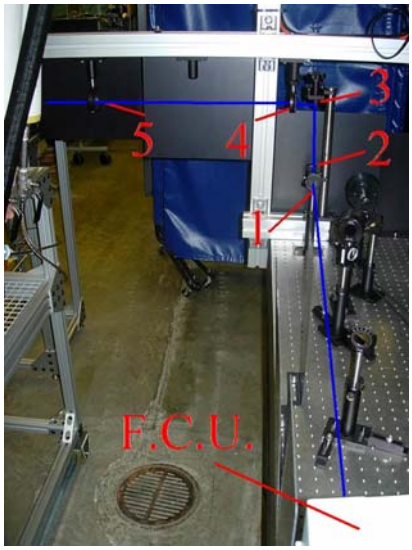

Fig. 21. Beam path part 1.

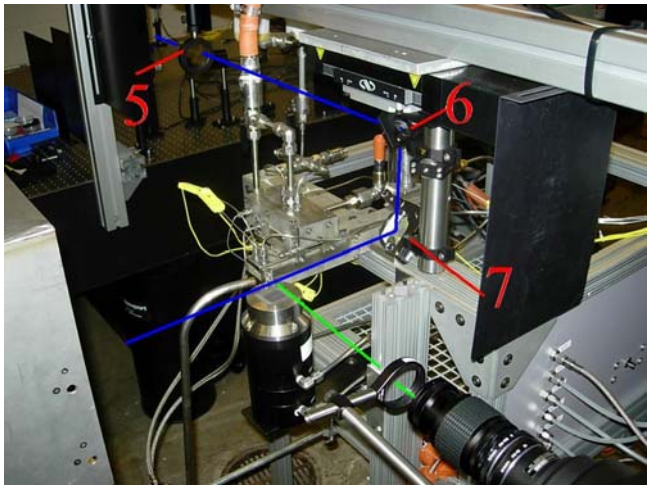

Fig. 22. Beam path part 2

Starting with Fig. 21, the beam leaves the frequency conversion unit and passes through an aperture (1) that blocks any residual light other than the primary beam. The beam then hits a 45° one inch diameter mirror (2) that reflects the beam upward where it hits a second 45° one inch diameter mirror (3) that reflects the beam along the Bosch support. The combination of these two 45° optics is commonly referred to as the periscope because it adjusts for height. The beam then passes through a cylindrical lens (4) with a focal length of -300 mm. The focal length is negative because instead of focusing the beam, the cylindrical lens diffuses the beam in one plane. The beam then passes through a spherical lens with a 1000 mm focal length labeled number five in both Fig. 21 and Fig. 22. The spherical lens focuses the beam into the thin sheet desired for LIF. The proper distance between the cylindrical lens (4) and the spherical lens (5) is simply the addition of their respective focal lengths which is:

$$-300 \text{ mm} + 1000 \text{ mm} = 700 \text{ mm}$$

The combination of the cylindrical and spherical lens is called the telescope. The beam which is now a thin sheet, leaves the spherical lens and moves toward the test subject.

The proper distance between the spherical lens and the burner is the focal length of the spherical lens which is 1000 mm. The thin sheet then hits another 45° one inch diameter mirror (6) where it is reflected down and then hits a final 45° two inch diameter mirror (7) that reflects it toward the burner. The last two 45° optics are attached to a translation stage that allow for spatial movements across any flame. Although the camera will be discussed in detail later, the green line in Fig. 22 shows the line of sight of the camera with respect to the laser sheet.

Measuring Wavelength and Power

As already mentioned, the laser beam leaves the dye laser at approximately 568 nm and enters the frequency conversion unit where the frequency is doubled to approximately 284 nm. However, the FCU is not 100% efficient so not all of the light is converted to 284 nm. Instead, there tends to be a residual 568 nm beam that also leaves the FCU on an off axis. This beam of residual 568 nm is reflected into fiber optic cable that feeds into a HighFinesse/Angstrom WS-7 Wavelength Meter shown in Fig. 23.

Fig. 23. Wavelength meter

The wavelength meter is connected to the computer in Fig. 19 and shows the real time wavelength within 0.0001 nm.

To measure the power of the 284 nm beam a power meter must be placed directly in the path of the beam. The power meter is connected to an Ophir Orion TH Handheld meter display which displays the power of the laser in mJ.

LIFBASE

Up to this point, it has been stated that the dye laser is tuned to approximately 568 nm. To determine this wavelength for OH LIF experiments a free software package known as LIFBASE is used. LIFBASE is a spectral simulation database for diatomic molecules published by Luque (Ref. 21). The theory behind LIFBASE can be found in Chapter 2, so this section will concentrate on the practical application and use of the software. Fig. 24 shows the input screen for LIFBASE once the program is opened.

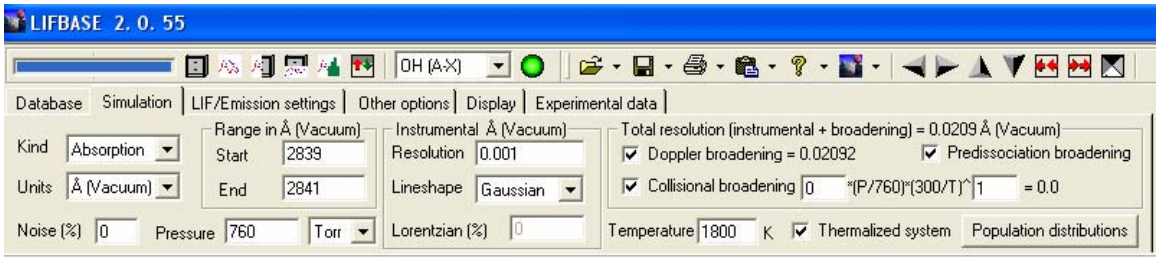

Fig. 24. LIFBASE input screen

Starting at the top of Fig. 24, there is a drop down menu next to the green button used to pick the desired molecule for simulation; the molecule chosen in the Fig. 24 is the OH (A-X) radical. The (A-X) is the electronic system where A is the excited state and X is the ground state. Starting from the left of the figure there is an option for the kind of simulation—either absorption or emission. The next box of inputs is the desired range of

the simulation, which in this case the simulation is set to run from 283.9 nm to 284.1 nm. The other important inputs are the pressure and temperature at the bottom of Fig. 24 which have a big impact on the simulation. To run the simulation, simply push the green button in the menu bar. The results of the inputs in Fig. 24 will result in the simulation pictured in Fig. 25.

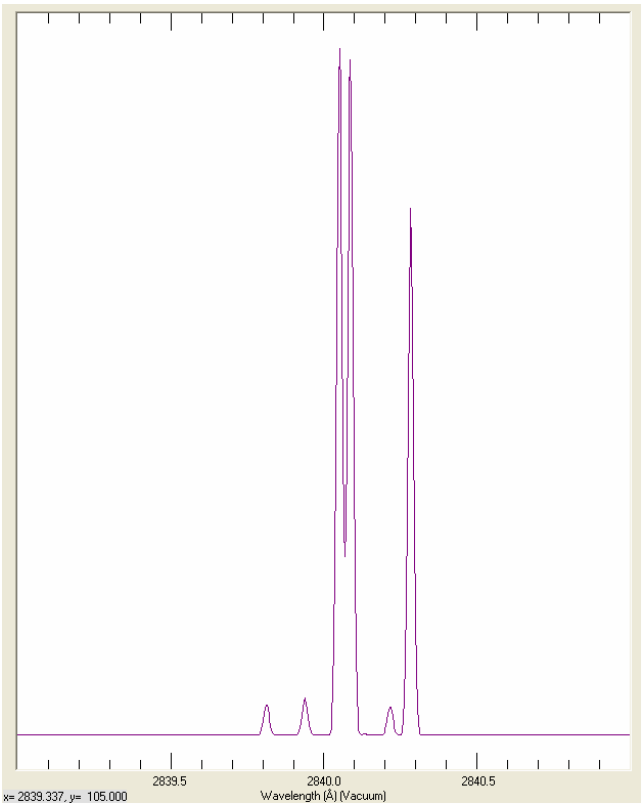

Fig. 25. LIFBASE absorption spectral simulation for OH at 1800K

The peaks in Fig. 25 represent the absorption wavelengths which will create an OH LIF signal. The best peak to use will be discussed further in the results section, but as expected the higher the peak the stronger the LIF signal will be.

Camera

The other vital component to the PLIF system is camera used to to capture up the OH fluorescent signal. The camera used in this lab is a Princeton Instruments Intensifying Charge Coupled Device (ICCD). Fig. 26 shows the camera:

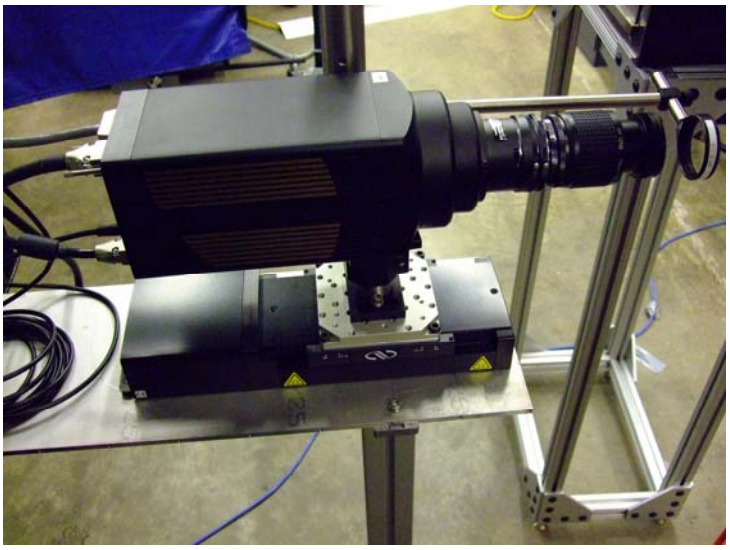

Fig. 26. Princeton Instruments ICCD camera

An ICCD camera is used because it has the ability to pick up very low light emissions. The light emitted by the excited OH radical passes through the lens of the camera and then into an intensifier. The intensifier is made up of a photo-cathode, a two-stage chevron micro-channel plate (CMCP), and Phosphor. The photon that enters the camera is absorbed by the photo-cathode and a single electron is released, the single electron the passes through small micro-channels of CMCP and the collisions with the walls channels cause multiple electrons to be released. The multiple electrons then hit the Phosphor where a photon is released for every electron. To summarize the intensifier, one photon produces one electron that produces multiple electrons in the CMCP, and the multiple electrons produce multiple photons when they come into contact with the Phosphor. So

for every one photon that enters the intensifier, multiple photons leave the intensifier. The photons then travel to the CCD portion of the camera where each photon is converted to an electron and the electrons are made into an image shown on the computer screen.

The camera is attached to a translation stage just like the final two mirrors that direct the laser sheet in Fig. 22. This combination of translation stages allows for the camera and beam to be moved simultaneously across any flame. The camera and translation stages are controlled by the computer on the small laser table shown in Fig. 27. The program that controls and operates the camera, WinView 32, is the same program that analyzes the images captured by the camera. The full start-up and shutdown procedures for the camera can be found in Appendix F.

Fig. 27. Camera control station

Hencken Burner

To test and calibrate the laser system a Hencken burner is used. The Hencken burner produces a laminar, premixed, and steady shaped flame. When conducting LIF on the flame produced by the Hencken burner it is assumed there are no perturbations in the

flame, therefore making any variations in measurements a result of the laser system. Fig. 28 shows the Hencken burner and the flame it produces.

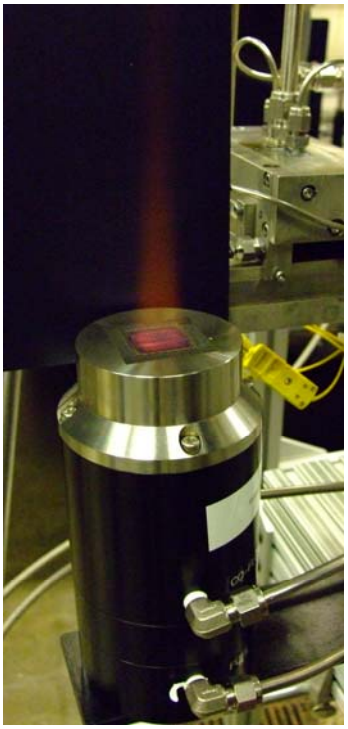

Fig. 28. Hencken burner

On the top face of the Hencken burner there are two squares. The inside square is where the mixed oxidizer and fuel is released for combustion and the outside square releases a co-flow around the flame. The co-flow acts as a protective barrier from interaction with outside air or other disturbances that may affect the flame. The fuel used for this experiment was pure hydrogen (H_2) since it produces a large concentration of OH radicals in the flame. The oxidizer used was zero air, which is bottled clean air with a very small amount of oil or other particulates. The co-flow can be any kind of inert gas and in this case pure nitrogen (N_2) was used. As previously mentioned the laser beam is focused into a thin sheet and sent through the Hencken flame. Fig. 29 shows a schematic of the flame and laser sheet interaction.

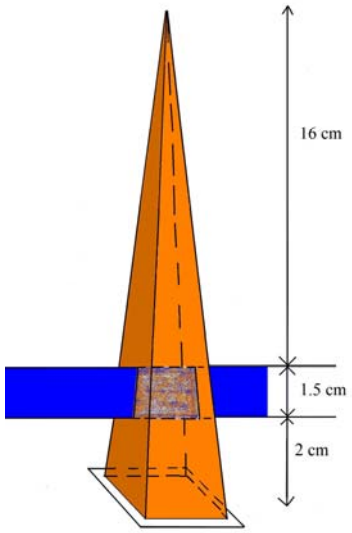

Fig. 29. Schematic of Hencken flame and beam interaction

Mass Flow Controllers

To accurately control the flow of the fuel, oxidizer and co-flow into the Hencken burner, four MKS ALTA digital mass flow controllers were installed. Fig. 30 shows the four mass flow controllers.

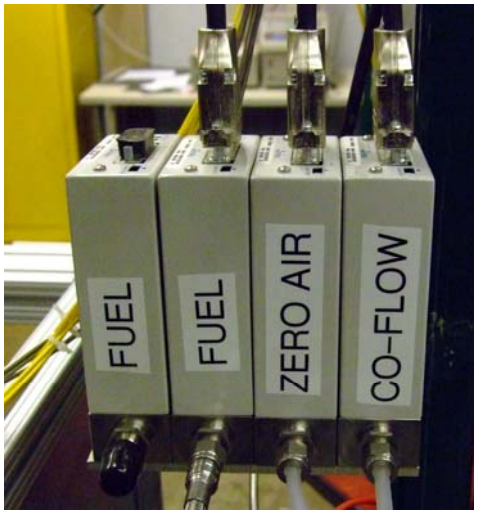

Fig. 30. MKS ALTA digital mass flow controllers

From left to right in Fig. 30 is a 5 standard liter per minute (SLPM) controller labeled “FUEL”, a 10 SLPM controller also labeled “FUEL”, a 20 SLPM controller labeled “ZERO AIR”, and a 30 SLPM controller labeled “CO-FLOW”. The digital mass flow controllers are wired into a MKS 247D Four Channel Power Supply/Readout shown in Fig. 31 and located at the computer control station.

Fig. 31. MKS 247D Four Channel Power Supply/Readout

Currently, the 10 SLPM fuel controller is wired into channel 1, the 20 SLPM zero air controller is wired into channel 2, the 30 SLPM co-flow controller is wired into channel 3, and there is nothing wired into channel 4. The display on the readout is a three or four digit percentage with a decimal point, for example if the controller read “956” it means 95.6%. Since the readout is in percentage, the mass flow controllers must be calibrated to calculate how percentage correlates with flow rate. To do this a BIOS International Corporation Definer 220-H shown in Fig. 32 was used.

Fig. 32. BIOS Definer 220H Flow Meter

To calibrate the controllers, simply disconnect the desired gas line downstream of the controller and insert it into the “pressure” connection of the BIOS mass flow meter, set the MKS 247D Readout in Fig. 31 to a desired percentage and log the corresponding mass flow rate from the mass flow meter. Once the points are taken, a line can be curve fit in order to interpolate every percentage based on the desired mass flow rate.

Currently the mass flow controllers are calibrated for hydrogen (H_2) as the fuel, zero air as the oxidizer, and nitrogen (N_2) as the co-flow. Flow points were taken at every 10% and the resulting in the following mass flow curves.

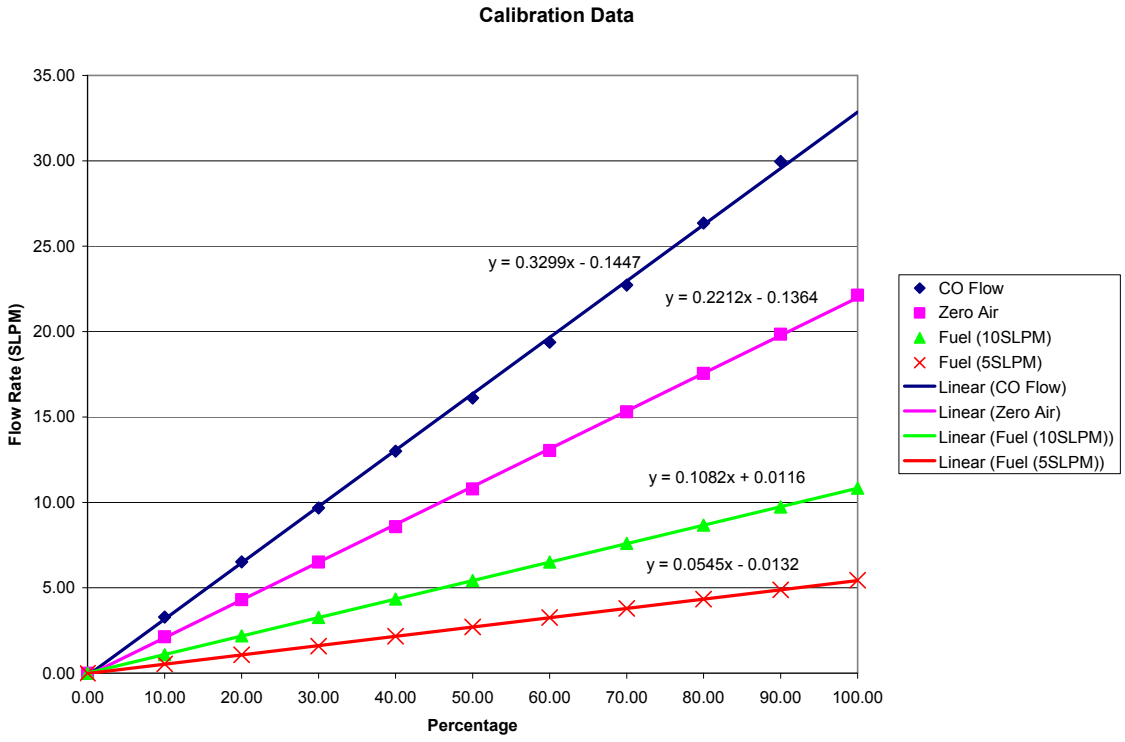

Fig. 33. Mass flow meter calibration data

Using the resulting equations in Fig. 33 a precise flow rate can be obtained for every percentage set on the MKS readout. This allowed for a variation in equivalence ratio for

the hydrogen-air flame from the Hencken burner since the equation for perfect combustion for a hydrogen-air flame is:

$$2H_2 + (O_2 + 3.76N_2) \rightarrow 2H_2O + 3.76N_2 \tag{3}$$

Therefore, the stoichiometric air to fuel ratio is:

$$\left(\frac{A}{F}\right)_{STOIC} = \frac{4.76}{2} = 2.38 \tag{4}$$

And equation for equivalence ratio becomes:

$$\phi = \frac{\left(\frac{A}{F}\right)_{STOIC}}{\left(\frac{A}{F}\right)_{ACTUAL}} = \frac{2.38}{\left(\frac{A}{F}\right)_{ACTUAL}} \tag{5}$$

Theoretical Equilibrium Data

The theoretical equilibrium data for the hydrogen-air flame was calculated at atmospheric temperature and pressure using STANJAN (Ref. 23). This data is necessary to provide a theoretical basis for the experimental results obtained through the OH PLIF of the Hencken flame. The desired information from STANJAN includes the temperature and OH concentration in a hydrogen-air flame for different equivalence ratios. For the reactants, the moles of air were held constant and the moles of hydrogen were varied according to equivalence ratio. The reactants and products input into STANJAN can be seen in Table 2.

Table 2. STANJAN inputs for hydrogen-air flame

Reactants		Products
symbol	**mols**	**symbol**
H_2	varied	H
O_2	1	O
N_2	3.76	N
CO_2	0.0016	H_2
		OH
		CO
		NO
		O_2
		H_2O
		CO_2
		N_2

Quenching

The definition and effects of quenching have been discussed in chapter 2, so this section will discuss how to actually calculate the quenching rate corrections. First the mole fractions of the products of combustion, adiabatic flame temperature (K), and the pressure (Pa) must be calculated using an equilibrium solver such as STANJAN. The constants needed for the quenching calculations are Boltzmann's constant, $k = 1.38065 \times 10^{-23} \frac{m^2 kg}{s^2 K}$, and the spontaneous emission constant for OH which is A= 1450000 s^{-1}. The parameters for the OH quenching rate shown in Table 3 are derived from Tamura et. al (Ref. 22).

Table 3. Quenching rate parameters from Tamura et al.(Ref. 22)

Colliding Species	$\sigma_{Q(INF)}$ (Angstroms)^2	ε/k (K)	Quenching Rate Coefficent m^3/s
CH_4	11.0	320	$(5.07\times10^{-19})(\sigma_Q)_(T^{0.5})$
H	14.5	84	$(15.0\times10^{-19})(\sigma_Q)_(T^{0.5})$
O	0.0	0	$(0\times10^{-19})(\sigma_Q)_(T^{0.5})$
N	0.0	0	$(0\times10^{-19})(\sigma_Q)_(T^{0.5})$
H_2	4.5	224	$(10.88\times10^{-19})(\sigma_Q)_(T^{0.5})$
OH	20.0	384	$(4.99\times10^{-19})(\sigma_Q)_(T^{0.5})$
CO	12.0	397	$(4.47\times10^{-19})(\sigma_Q)_(T^{0.5})$
NO	0.0	0	$(0\times10^{-19})(\sigma_Q)_(T^{0.5})$
O_2	8.0	243	$(4.37\times10^{-19})(\sigma_Q)_(T^{0.5})$
H_2O	20.0	434	$(4.92\times10^{-19})(\sigma_Q)_(T^{0.5})$
CO_2	11.0	488	$(4.16\times10^{-19})(\sigma_Q)_(T^{0.5})$
N_2	0.4	624	$(4.47\times10^{-19})(\sigma_Q)_(T^{0.5})$

The steps to calculating OH LIF efficiency are:

1. Calculate the temperature dependence of the cross sections for each molecule (21).

$$\sigma_Q = \sigma_{Q(INF)} e^{\left(\frac{\varepsilon}{kT}\right)} \tag{6}$$

2. Calculate the quenching rate coefficient for each molecule listed in Table 3 using the equations in the fourth column of Table 3.

3. Calculate the species number density for each species

$$\textit{Species Number Density} = \textit{(mol fraction of the species)}\left(\frac{P}{kT}\right) \tag{7}$$

4. Calculate the quenching rate for each species

$$Q_{each\_species} = \textit{(Species Number Density)(quenching rate coefficient)} \tag{8}$$

5. Add the quenching rates for each molecule to get a total quenching rate

$$Q_{TOTAL} = \sum Q_{each\_species} \tag{9}$$

6. Calculate LIF Efficiency

$$LIF\ Efficiency = \frac{A}{\left(A + Q_{TOTAL}\right)} \tag{10}$$

The LIF Efficiency is used to normalize the signal from the experimental data and is discussed fully in the results section below.

IV. Results and Discussion

4.1 Facility Validation

The AFIT combustion lab is a state of the art facility and is ready to test the sectional ultra-compact combustor models. The lab also provides the flexibility and capability to support future combustion research. The major steps forward in the combustion laboratory are the operability and practical use of all of the major hardware components.

The infinite radius UCC rig is in place and ready for testing. All fuel, air, and instrumentation lines have been plumbed and the rig is ready for testing. All connections to both the stand and combustion rig are Swagelock compression fittings to allow for easy changes in the system. The heaters are operational and can be controlled at the computer control station. When the heaters became operational, heated air was run through the UCC rig. Fig. 34 shows the temperature profile at the inlet and exit of the main vane of the sectional UCC as a function of time.

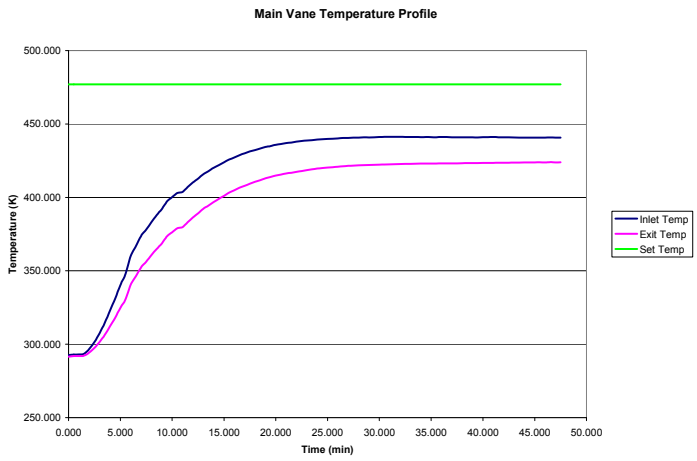

Fig. 34. Main vane temperature profile

Fig. 35 shows a similar plot of the cavity temperature profile as a function of time.

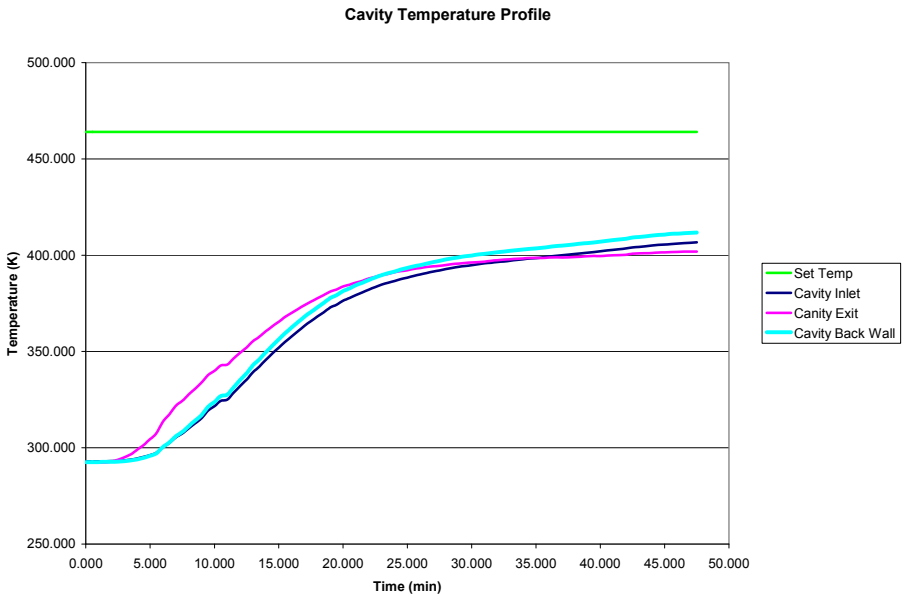

Fig. 35. Cavity temperature profile

These plots are significant because they are the first data ever taken using the data acquisition system. These plots validate the data collection abilities of the LabView VI created by Anderson (Ref. 5) and functionality of the thermocouples and connections on the combustor. These plots also show there is approximately a 50 K drop in temperature between the set point of the heaters and temperature of the air delivered to the combustor. The plots in Fig. 34 and Fig. 35 show it takes approximately 25-30 minutes for the combustion rig to warm up and reach a steady state condition. The slopes of the lines for the temperatures of the main vane and cavity differ slightly because the extra precaution must be taken when heating the air in the secondary line heater. When a low flow rate is used, approximately 1 kg/min and less, the heater needs to be watched closely because it

has a tendency to overheat. To overcome this, the initial set point of the secondary heater should be set to a lower value and slowly increased to the desired temperature. This is why the temperatures in Fig. 35 take longer to reach a steady state condition.

The other data taken with heated air through the combustor was the pressure at the main vane and cavity inlet and exit shown in Fig. 36.

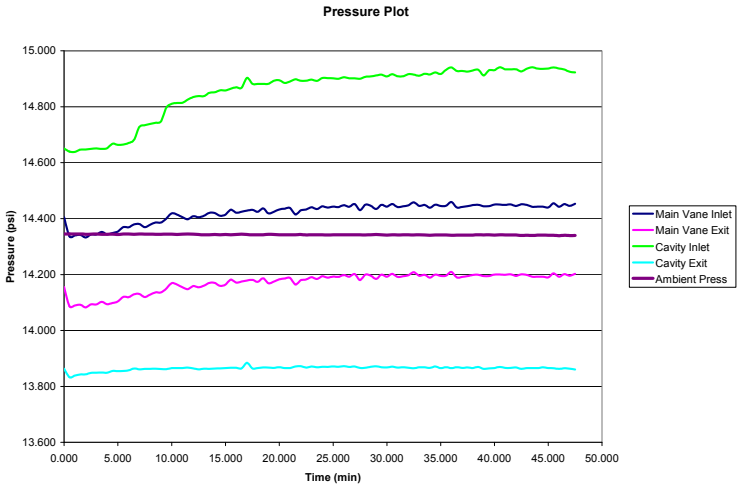

Fig. 36. Pressure profile for heated air experiment

Just as the temperature profiles validated the connection of the thermocouples and wiring, the pressure profile validates the pressure taps and pressure transducers in the lab. The shape of the pressure profile mirrors the temperature profiles, which is expected since temperature and pressure are related.

The exhaust system has successfully been installed, tested, and is ready for use. The exhaust hood and horizontal catch provide more than enough air flow for the UCC sectional rig experiments and combustion experiments in the future. The horizontal catch can be rotated and oriented in various positions to allow a range of different experiments. This coupled with the modular design of the combustion stand and ease of movement

allow for a wide variety of future experiments such as rocket motors and other combustion devices.

Most of the emissions collection system has been tested and is ready for use. The Mokon Compact Heated Thermal Fluid System has been cleaned, filled, purged and tested. The complete operating guide can be found in Appendix E. All of the Watlow tube heaters have been wired and are ready for use.

Most importantly, the lab and tank farm have been certified for combustion experiments through official channels. The front and back door in the lab have been replaced with fire proof doors and every pipe or opening that comes through the wall into the lab has been protected by fire proofing material. All combustible gas and carbon monoxide devices have been installed and are ready for use.

To summarize, every major component in the AFIT combustion lab has been turned on, tested, and properly controlled. Testing is ready to commence on the UCC sectional rig and future experiments. The detailed start-up and shutdown procedures for the lab can be found in Appendix E.

4.2 LIF Results

The major results of any OH LIF combustion experiment are the OH concentration in the flame and temperature of the flame. When starting a new lab, such as the case for the AFIT combustion facility, it is necessary to test the laser system on a flame that the properties are well known. Hence, a Hencken burner was used because it provides a premixed, laminar, steady flame. Therefore, any fluctuations in the OH data from the LIF measurements can be assumed to be from the laser system and not from variations in the flame.

Results of basic setup for OH LIF

The first step of the experiment is to find the equilibrium temperature in the hydrogen-air being used in the Hencken burner. As mentioned in chapter 3, the equilibrium software used was STANJAN (Ref. 23) and varying the equivalence ratios in the program resulted in the adiabatic flame temperatures shown in Fig. 37. The data points that were calculated are connected with a curve fit line.

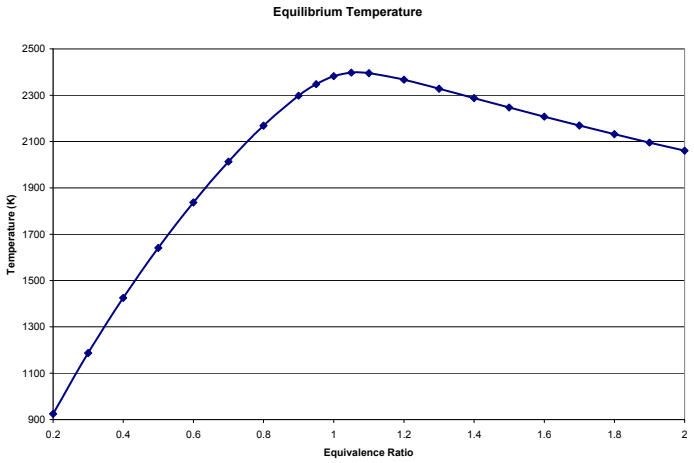

Fig. 37. Equilibrium temperature of a hydrogen-air flame

The second step to obtaining OH LIF results is to find the correct wavelength using LIFBASE (Ref. 21) that will create a strong OH signal that the ICCD camera can image. The use of LIFBASE is discussed in detail in chapter three and the result of the program is a plot of a series of distribution curves with peaks at particular wavelengths. The Boltzmann distribution determines the of number of molecules in each state. From Table 1, the full range of electronic transition for the OH radical is between 240 nm to 400 nm. Running LIFBASE over this range results in the spectrum pictured below in Fig. 38.

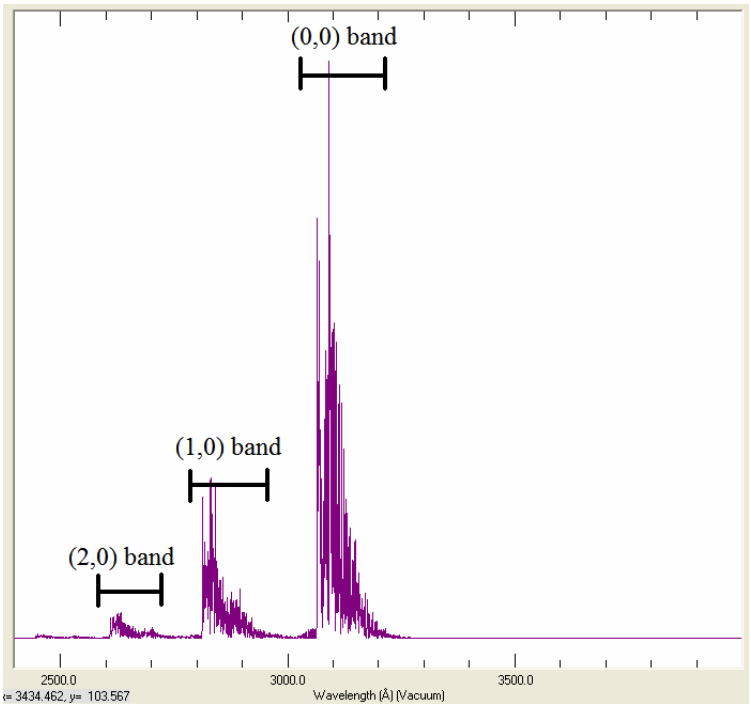

Fig. 38. Full range of OH absorption at 2400 K from 240 nm to 400 nm

Fig. 38 shows that there are three bands of OH A-X electronic transition, the first is the (0,0) band with a peak around 308 nm, the second is the (1,0) with a peak around 284 nm, and the much smaller third band is the (2,0) band centered around 263 nm. The magnitude of the peaks on the LIFBASE output vary as the input temperature is changed. As mentioned, the Boltzmann fraction governs the distribution of the molecules and it is dependent on temperature. The wavelength that creates the most desirable OH LIF signal is the wavelength that has a strong peak and is the least sensitive to temperature. From previous experience with the Hencken burner, it is known that the practical limits of the flame are equivalence ratios between 0.5 and 1.4. Anything below $\phi = 0.5$ is hard to keep the flame lit, and above $\phi = 1.4$ the screens on top of the Hencken flame start to glow red and has the potential to cause damage to the burner. Going back to the flame temperature from STANJAN in Fig. 37 the effective temperature range for an

equivalence ratio of 0.5 to 1.4 for a hydrogen-air flame is approximately 1500 K to 2500 K. Therefore, the best wavelength from LIFBASE is the peak that is the least sensitive between 1500 K and 2500 K. Fig. 39 shows the temperature dependence of various OH absorption lines and was provided by Meyer (Ref 24).

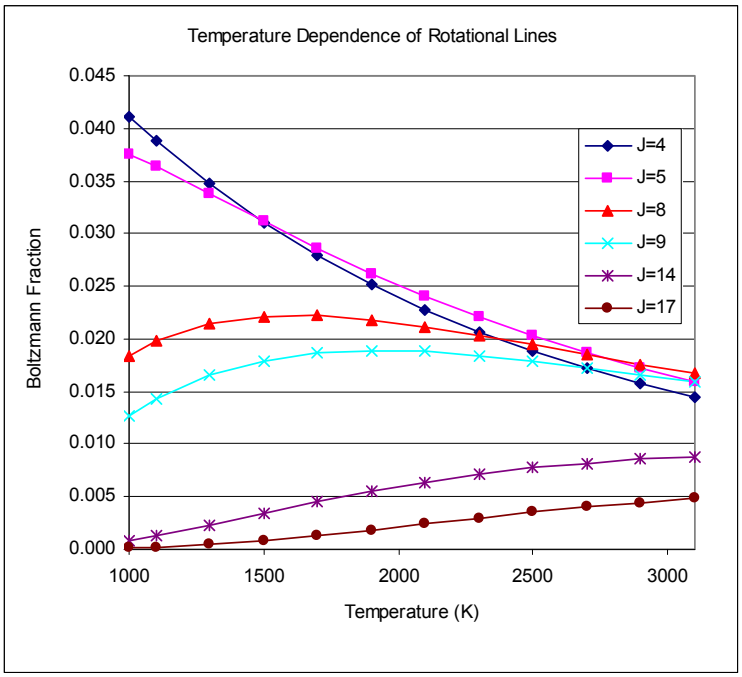

Fig. 39. Temperature dependence of various LIFBASE lines. Provided by Meyer (Ref. 24).

Figure 39 shows that over a temperature range of 1500 K to 2500 K, the J = 9 and the J = 8 lines are the least sensitive. The J = 9 line is the line that corresponds with a wavelength of 284.005 nm. Even though the peak around 308 nm is higher, the peak at 284.005 nm is used because it is the most temperature insensitive. In summary, the primary excitation wavelength used for OH LIF in this experiment was 284.005 nm because it is the strongest peak that is the most insensitive to temperature. Spectroscopically, this means excitation will occur in the (1,0) vibrational band in the A-X electronic system.

Recalling Fig. 6b, light is emitted at the same and higher wavelengths of excitation. Running LIFBASE over the same 240 nm to 400 nm electronic transition range for OH produces the emission spectra in Fig. 40.

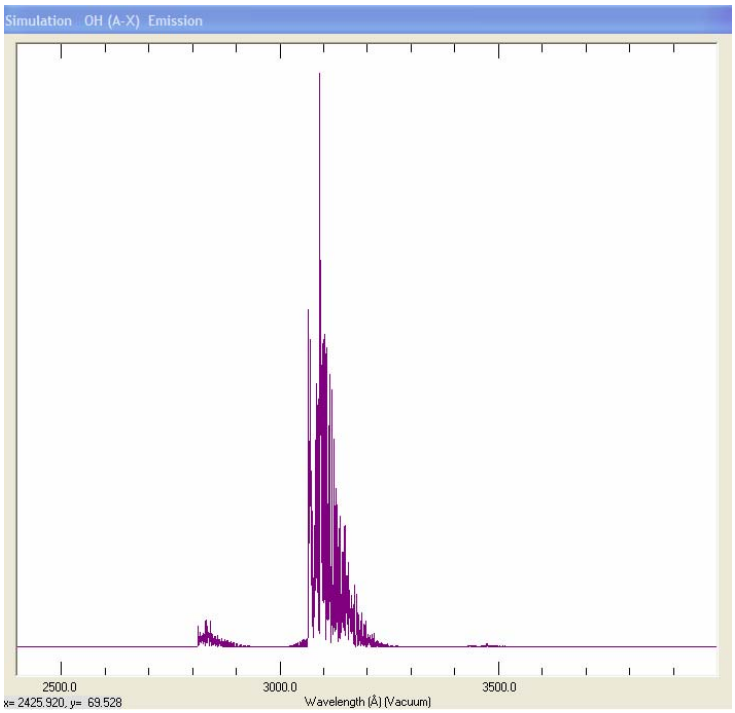

Fig. 40. OH emission spectra at T = 2300 K

The emission spectra in Fig. 40 has the same (0,0) and (1,0) vibrational bands as the absorption spectra in Fig. 38. Since the OH molecule will be excited at 284.005 nm, light will be emitted in the (1,0) band at and above 284.005 nm and over the entire (0,0) band. When detecting the emitted light it is often desirable to detect as much of the emission spectra as possible without detecting the laser. If the laser is detected, the intensity of the detected signal will be a combination of the laser light and the OH fluorescence, instead of only the OH fluorescence. To ensure the laser is not detected, a filter is used in front of the camera to block the wavelength of the laser. The filter used in this experiment is a Schott Colored Glass filter. More specifically, the filter was a Schott CG-WG-295. The

CG simply means Colored Glass, the WG means it is White Glass, and 295 means that 295 nm is the 50% transmittance point of the filter. According to the information published by Schott (Ref. 25), the CG-WG-295 only transmits approximately 1% of the light at 284 nm and, 50% at 295 nm, and 95% by 325 nm. Therefore, the laser is blocked and the fluorescent emission in the (0,0) band is detected.

Summarizing this process, the OH molecule is excited at 284.005 nm which is in the (1,0) band in the (A-X) electronic system. To stop the laser from being detected with the fluorescent signal, a filter is used to block the laser light. Finally, detection occurs over the entire (0,0) band. This summary is depicted in the OH emission spectra in Fig. 41. The blue line represents the excitation wavelength of 284.005 nm and the red line represents the filter transmittance based on published information from Schott Glass (Ref. 25).

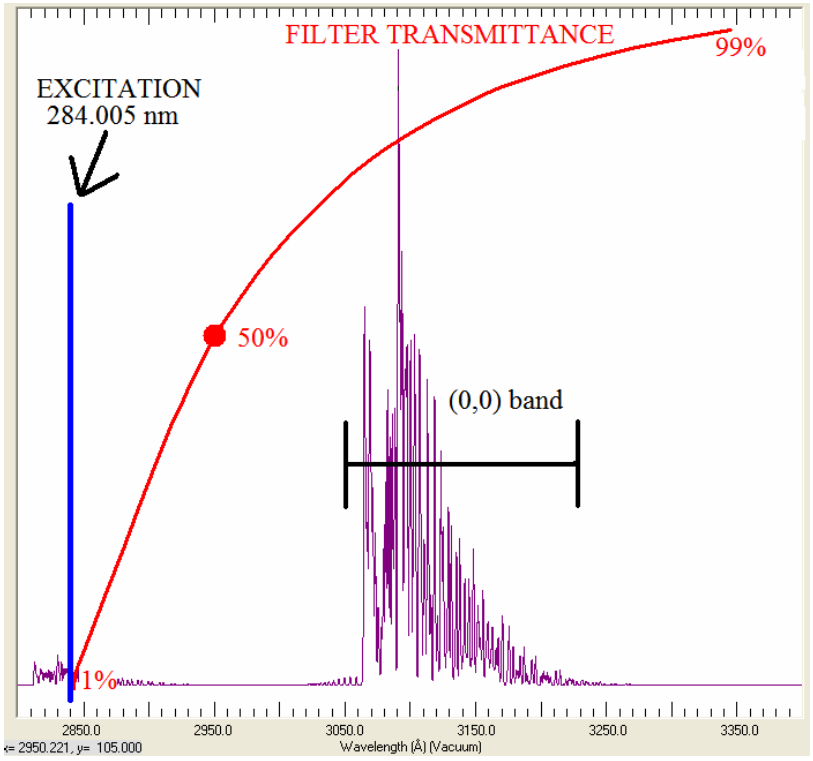

Fig. 41. Excitation and detection process summary

The dye laser was tuned to output a wavelength of 284.005 nm and the camera was focused on the center of the interaction of the Hencken flame and laser. The dimensions of the images produced by the camera as well as the relative dimensions of the laser and flame interaction are shown in Fig. 42. In Fig. 42, the orange represents the flame, the blue represents the laser going through the flame, and the white is the intersection of the two and where the OH signal is produced.

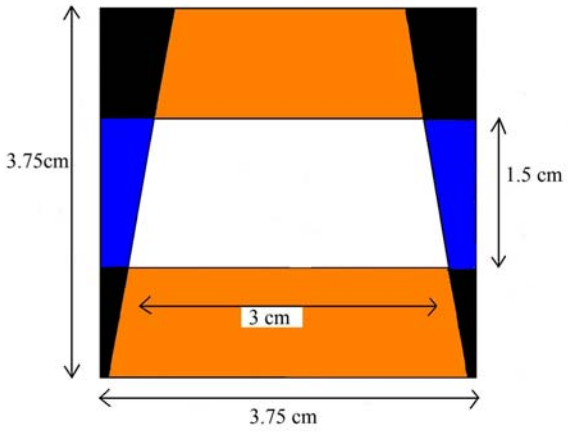

Fig. 42. Image dimensions with the interaction of the Hencken flame and laser sheet

An actual image captured by the camera is shown below in Fig. 43.

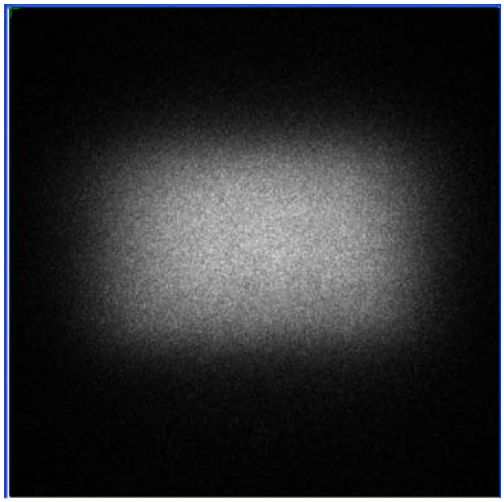

Fig. 43. Actual camera image

The white mass in the center of the image in Fig. 43 is the instantaneous fluorescent OH signal.

With the wavelength set at 284.005 nm, images were collected down the center of the flame for equivalence ratios between 0.6 and 1.3. For every change in equivalence ratio, 50 images were captured at 10 hertz to provide continuity in data collection and analyzation. After images were taken for all equivalence ratios, 50 images were captured with no flame to create a background image. All 50 images for both the flame data and the background were then averaged to produce one image for every setting. The background image was subtracted from the other images to remove any background noise. The result of an image being averaged and the background removed can be seen below in Fig. 44.

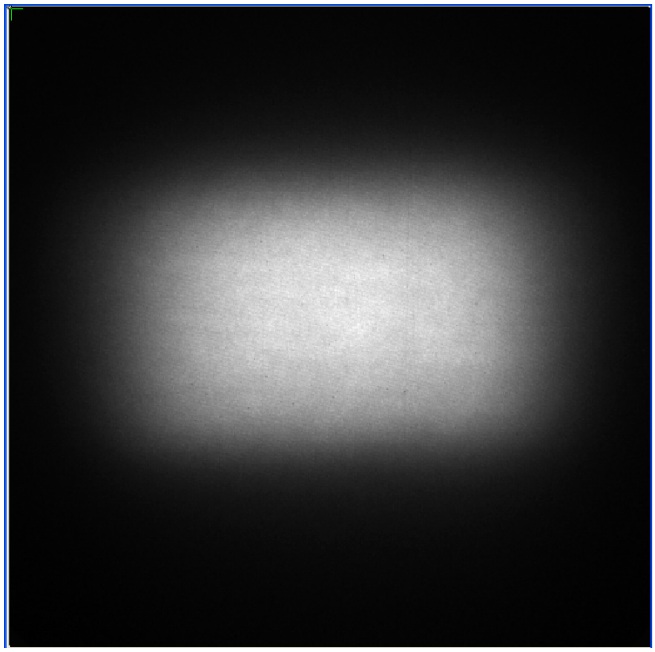

Fig. 44. Typical averaged image minus the background

Intensity variation as a function of length

The top and bottom edges of the fluorescent signal in Fig. 43 and Fig. 44 are not well defined because the edges of the laser sheet are not perfectly focused. Similarly, the left and right edges of the signal are not well defined because of interaction of the laser with edge of the flame. Therefore, the first step in data reduction was to find out exactly how the averaged images vary across the entire x- and y-plane to determine the most suitable area for statistical analysis. The images were converted to a text file so that the intensity across the center of the flame in both the x- and y- planes could be easily be plotted. The desired area for statistical analysis occurs where the intensity is the greatest and most constant. Fig. 45 shows the variation in the x-direction for an equivalence ratio

of $\phi = 1.0$. The area between the two red lines is area in the x-direction chosen for the analysis of all images throughout all experiments.

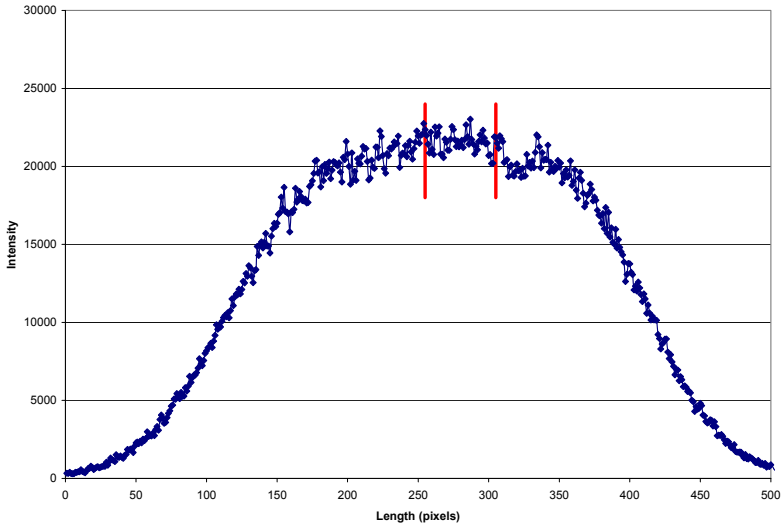

Fig. 45. Intensity variation in the x-direction through the center of the laser sheet

Fig. 46 shows the intensity variation in the y-direction in the center of the image. Here too, the area between the red lines shows the region chosen for analysis for all images throughout the experiment.

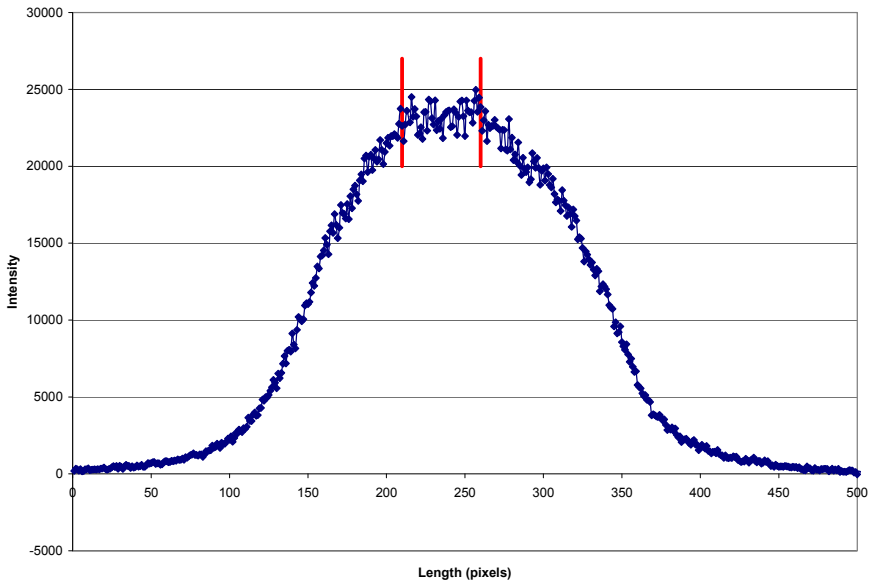

Fig. 46. Intensity variation in the y-direction through the center of the flame

To put the areas between the red lines in Fig. 45 and Fig. 46 in perspective, Fig. 47 shows the area on the schematic of the laser and flame interaction. The 3.5 mm square in the middle of the flame is the chosen area of analysis for all images.

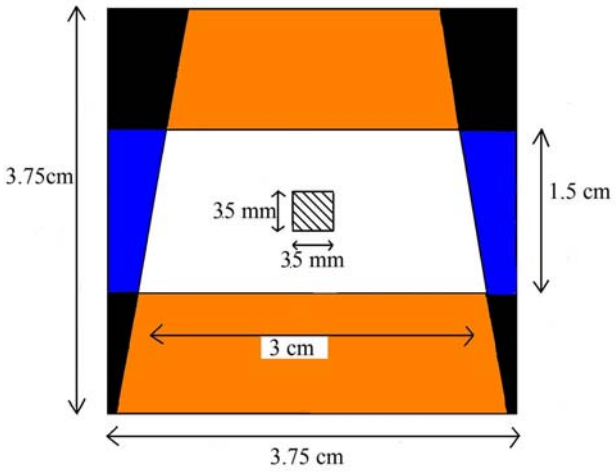

Fig. 47. Schematic of analysis area for all images

System uncertainty

Since it is assumed there are no perturbations in the Hencken flame, any variations in the images is assumed to be due to changes in the laser system. To quantify this uncertainty, a statistical analysis of all 50 unaveraged images in the 3.5 mm area of interest for various equivalence ratios was performed. First the average intensity for all fifty images was calculated and plotted. The average intensity for an equivalence ratio of $\phi = 1.0$ is show below in Fig. 48.

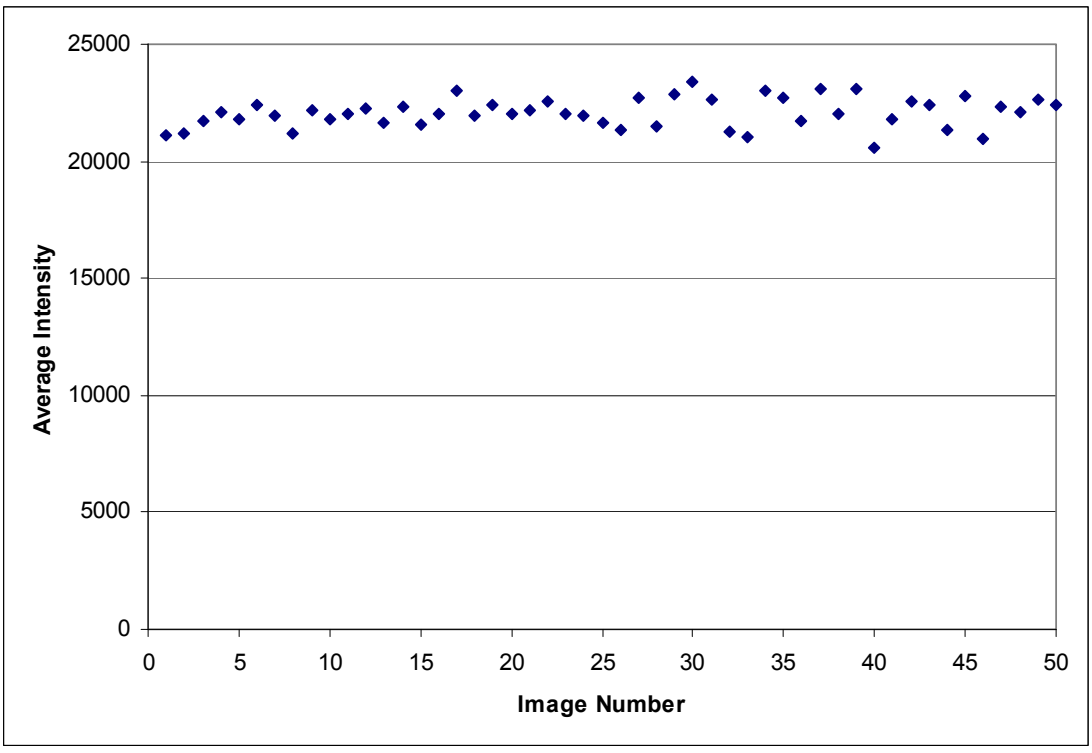

Fig. 48. Average intensity for 50 images at an equivalence ratio of 1.0

To calculate the uncertainty, the standard deviation for the fifty images was divided by the average intensity for all fifty images for numerous equivalence ratios. This resulted in an average system uncertainty of 2.5%.

Concentration Data

The primary reason for performing any OH LIF experiment on a flame if to find the OH concentration in the flame. The LIF signal intensity is directly proportional to the concentration of OH in the flame. In other words, the greater the intensity of the image the greater the OH concentration. The theoretical concentration of the OH radical in a hydrogen-air flame was calculated using STANJAN equilibrium software. According to theoretical data, the concentration varies with equivalence ratio with a maximum occurring at $\phi = 0.95$. The concentration of OH in parts per million (ppm) as a function of equivalence ratio is shown in Fig. 49.

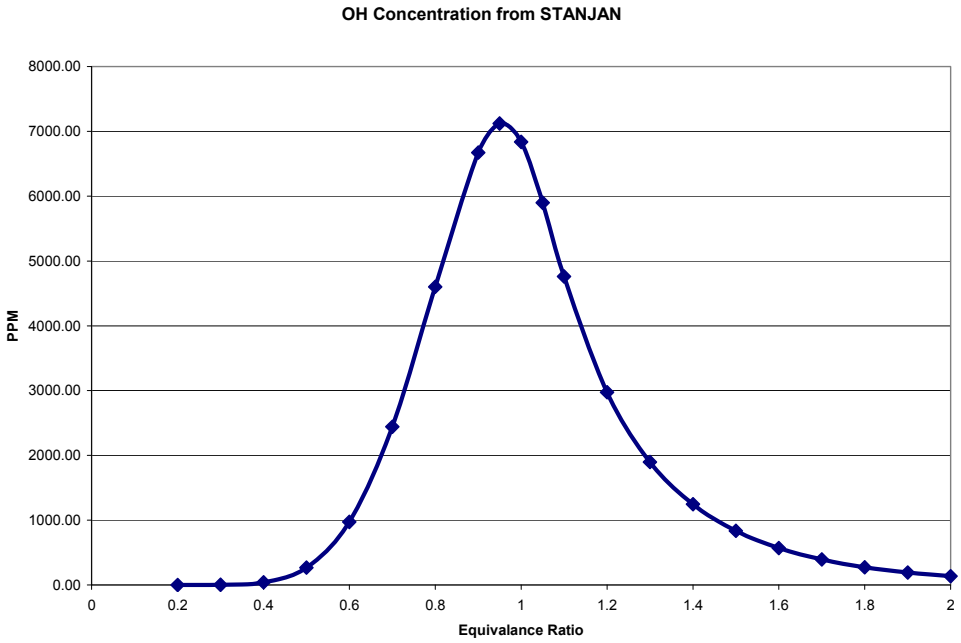

Fig. 49. Theoretical OH concentration from STANJAN

The intensity for the averaged images of equivalence ratios between $\phi = 0.6$ and $\phi = 1.3$ was calculated and then normalized by the greatest intensity. The averaged

intensities where then plotted against the theoretical OH concentrations by matching the maximum values as shown in Fig. 50.

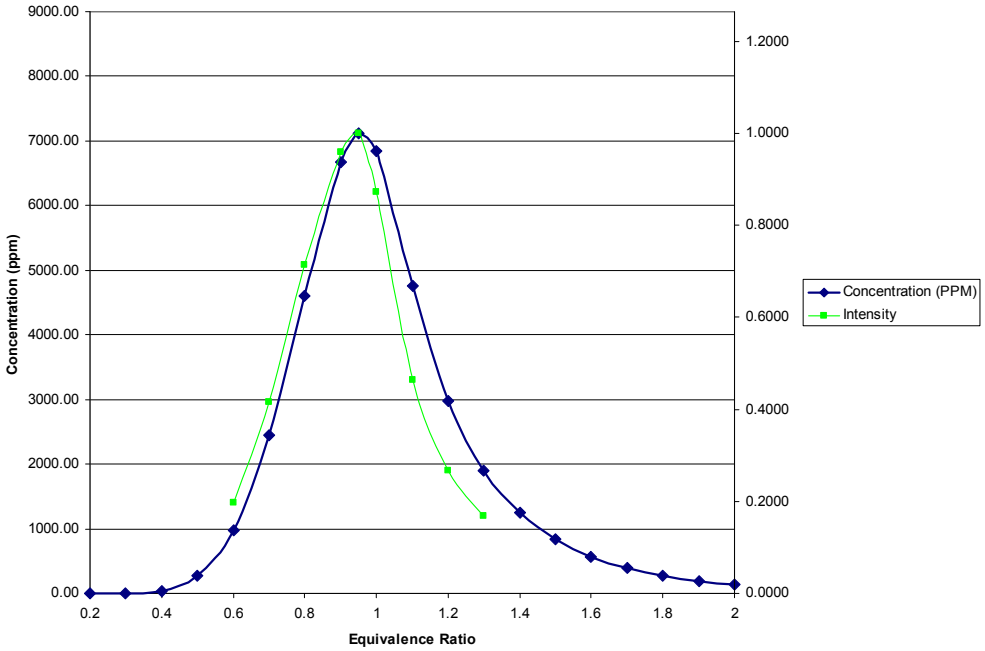

Fig. 50. Experimental intensity and theoretical OH concentration

The plotted experimental data has the same shape as the theoretical data but there is obviously some error as the intensity gets further away from the maximum value of $\phi = 0.95$.

As previously discussed, some of this error is due to the quenching that occurs with other molecules. Using the method discussed in Chapter 2, the LIF efficiencies due to quenching for OH in a hydrogen-air flame are listed in Table 4. OH LIF efficiencies for a hydrogen-air flame. A full table of the mole fractions of products used for the LIF efficiency calculations can be found in Appendix D.

Table 4. OH LIF efficiencies for a hydrogen-air flame

φ	LIF Efficiency
0.2	0.00264
0.3	0.00271
0.4	0.00270
0.5	0.00265
0.6	0.00259
0.7	0.00252
0.8	0.00244
0.9	0.00236
0.95	0.00233
1	0.00229
1.1	0.00224
1.2	0.00219
1.3	0.00215
1.4	0.00211
1.5	0.00207
1.6	0.00204
1.7	0.00200
1.8	0.00197
1.9	0.00194
2	0.00191

To use this data, the averaged intensities for the experimental data for each equivalence ratio are divided by the LIF efficiency for the respective equivalence ratio.

$$Corrected\ Singal = \frac{Average\ Intensity}{LIF\ Efficiency} \tag{11}$$

The corrected signal can then be normalized and plotted against the theoretical concentrations. Fig. 51 shows the theoretical data, the uncorrected normalized intensities, and the quenching corrected normalized intensity.

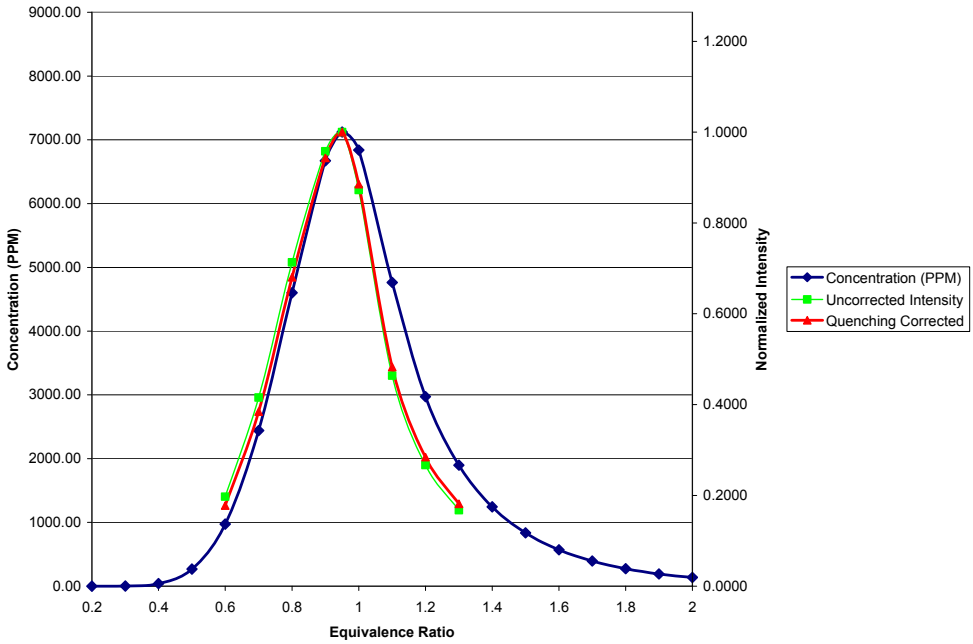

Fig. 51. Quenching corrected experimental data and theoretical OH concentration

The correction for quenching does improve the error between the theoretical concentration data. Table 5 shows the percent error between the theoretical concentration and uncorrected intensity; and the theoretical concentration and quenching corrected signal.

Table 5. Percent error between theoretical concentration and uncorrected and quenching corrected intensity

φ	Percent Error	
	Uncorrected	Corrected for Quenching
0.6	44%	30%
0.7	21%	12%
0.8	10%	5%
0.9	2%	1%
0.95	0%	0%
1	9%	8%
1.1	31%	28%
1.2	36%	32%
1.3	37%	32%

The quenching correction does reduce the error between intensity and theoretical concentration by up to 50%. Overall, the fuel lean equivalence ratios are much more accurate than the fuel rich equivalence ratios. The most likely explanation for this inaccuracy is the location of the laser in relation to the top of the burner. As Fig. 29 shows, the laser is approximately two centimeters above the top of the Hencken burner. This is significant because the quenching rate is very dependent on the height above the burner because mixing of the species and temperature depend on where in the flame the LIF measurements are made (Ref. 22). In other words, the error in the fuel rich equivalence ratio data is still due to quenching because the coefficients used to calculate quenching rate are assumed to be constant when in reality they vary throughout location of the flame.

Flame Temperature

The other goal is to determine the temperature of the flame from the OH LIF signal. Calculating the temperature is based on ratios, starting with the ratios of peaks within LIFBASE. As mentioned earlier, the magnitude of the peaks in a LIFBASE simulation will vary according to the input temperature. So, the first step to calculating actual temperature in the flame was to run the LIFBASE simulation over the range of expected flame temperatures. When LIFBASE displays the data, it normalizes the magnitude of the peaks with the largest peak. In other words, the highest peak on the screen will have the magnitude of 100 and the other peaks will be normalized by that value. Since the peaks are normalized it is the ratio of the peaks that is used to predict the actual temperature in the flame. Since the peak at 284.005 nm was used in the rest experiment, the lines surrounding the wavelength were used for ratios. The LIFBASE

simulation was run for a wavelength range of 283.9 to 284.1 nm over the expected temperature range of 1500 K to 2500 K at 50 K increments. The results of the simulation at T = 1800 K and T = 2400 K are displayed below in Fig. 52 and Fig. 53. Notice that the peak at 284.0050 nm is the tallest at 100, but the peaks at 284.0086 and 284.0283 are different for the two temperatures.

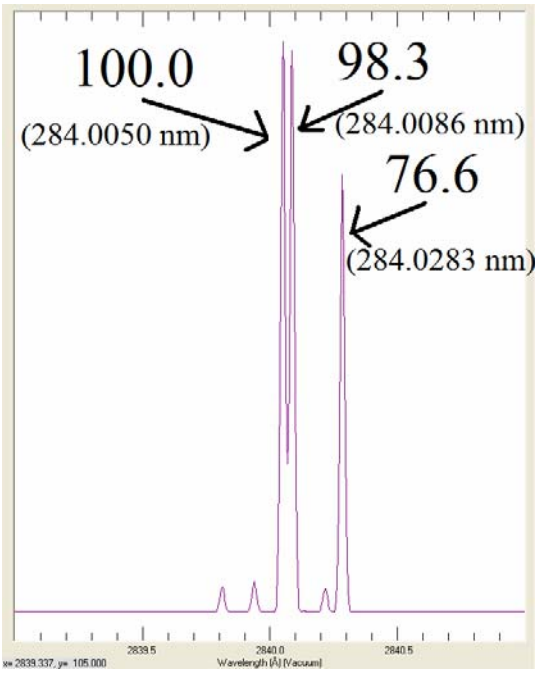

Fig. 53. LIFBASE simulation at T = 1800 K

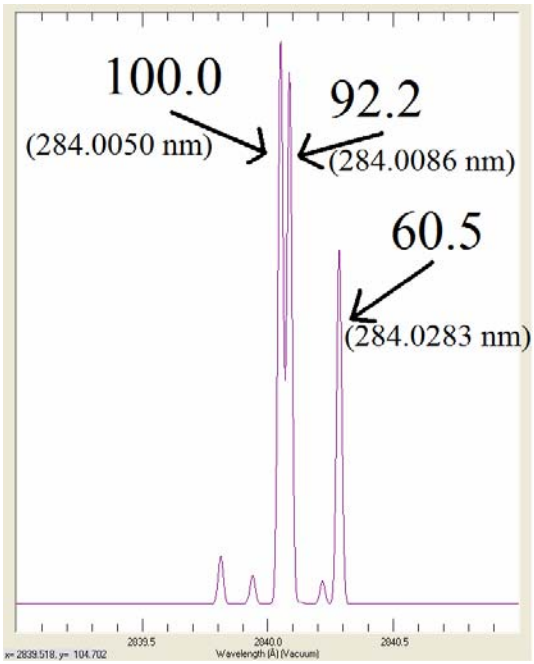

Fig. 52. LIFBASE simulation at T = 2500 K

The ratio of the peaks at 248.008 nm and 284.005 nm and between 284.028 nm and 248.005 nm were taken across the entire temperature range and results are in Table 6.

Table 6. LIFBASE ratios of peak magnitudes

Temperature	Ratio= $\frac{284.008\ nm}{284.005\ nm}$	Ratio= $\frac{284.023\ nm}{284.005\ nm}$
1500	1.0253	0.9184
1550	1.0218	0.8857
1600	1.0133	0.8565
1650	1.0140	0.8391
1700	0.9875	0.8051
1750	0.9900	0.7862
1800	0.9835	0.7663
1850	0.9808	0.7506
1900	0.9748	0.7284
1950	0.9664	0.7179
2000	0.9536	0.7010
2050	0.9557	0.6876
2100	0.9518	0.6741
2150	0.9496	0.6549
2200	0.9467	0.6585
2250	0.9347	0.6382
2300	0.9442	0.6282
2350	0.9304	0.6173
2400	0.9215	0.6048
2450	0.9244	0.6019
2500	0.9229	0.5966

This table of ratios and temperatures essentially becomes a thermometer for ratios of signal strength for values at the three chosen wavelengths.

The next step to calculating the temperature was to capture and analyze images at $\phi = 0.8$, $\phi = 0.9$, $\phi = 1.0$, and $\phi = 1.1$ at the same wavelengths that the LIFBASE ratios were calculated—which were 284.0050 nm, 284.0086 nm, and 284.0283 nm. It is important to note, that when changing the actual laser wavelength the power of the laser will fluctuate and it is important to test and write down the power before calculating the intensity data for that particular wavelength. The goal is to have the changes in intensities be only a function of the changes in wavelength and not laser power. Therefore, once all the data is collected the intensities are divided by the laser power to normalize the data and remove any fluctuation.

Finally, the ratio of intensities are taken in the same manner as the ratio of peaks in Table 6. The ratio of intensities are then compared to the ratios of peaks in Table 6 to

find the temperature for that corresponding ratio. Overall, the raw experimental temperatures were approximately 200 K low. Based on justification from Seitzman et al. (Ref. 26) the temperatures were scaled by a calibration constant of 1.14 to match the theorectical data. The resulting temperatures of this method are shown below in Table 7.

Table 7. Experimental flame temperatures

	Ratio= $\frac{284.008\ nm}{284.005\ nm}$	Ratio= $\frac{284.023\ nm}{284.005\ nm}$	Average Temperature (K)	Scaled Temperature (K)
φ=.8	2319	1553	1936	2207
φ=.9	2319	1710	2014	2296
φ=1.0	2298	1856	2077	2368
φ=.1.1	2166	1779	1973	2249

Fig. 54 shows the theoretical and scaled experimental temperatures.

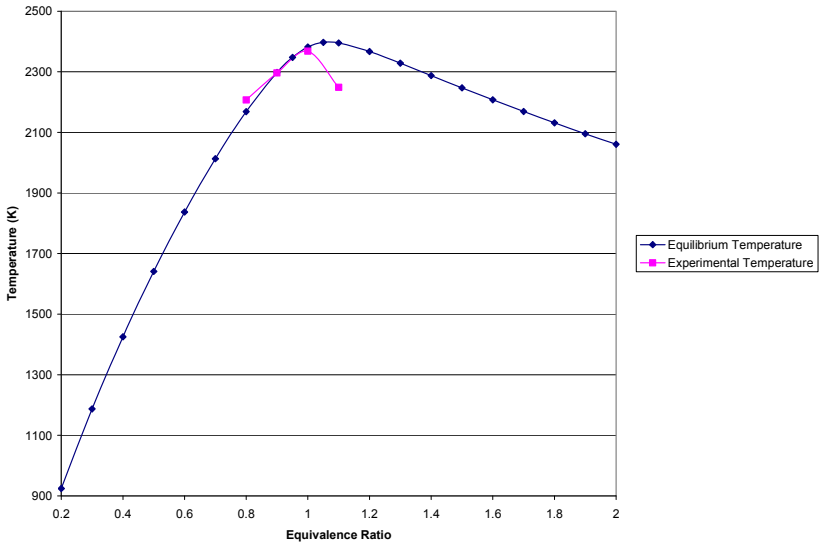

Fig. 54 Theoretical and experimental flame temperature

Similar to the concentration data, the temperatures matched the fuel lean equivalence ratios very well. Quenching is not taken into account because it is the same for the various equivalence ratios. The sources of error for this is method are similar to the sources of error for the concentration data. The data is being taken approximately

two centimeters from the top of the burner where mixing and entrainment from the nitrogen co-flow can occur. This mixing explains why the experimental temperature at $\phi = 1.1$ is lower than the equilibrium temperature even after the correction factor is added.

Spatial Data

As already mentioned, the camera and final two mirrors that direct the laser sheet toward the Hencken burner are attached to translation stages. This allows the position of the laser sheet and the camera to move in tandem spatially across the flame. This ability to move spatially will really be useful when testing the UCC and other combustion devices because it adds the third dimension to the two dimensional LIF measurements. A spatial profile was performed on the Hencken burner to essentially validate the method at equivalence ratios of $\phi = 1.0$ and $\phi = 1.2$. The results of the spatial profile are shown in Fig. 55.

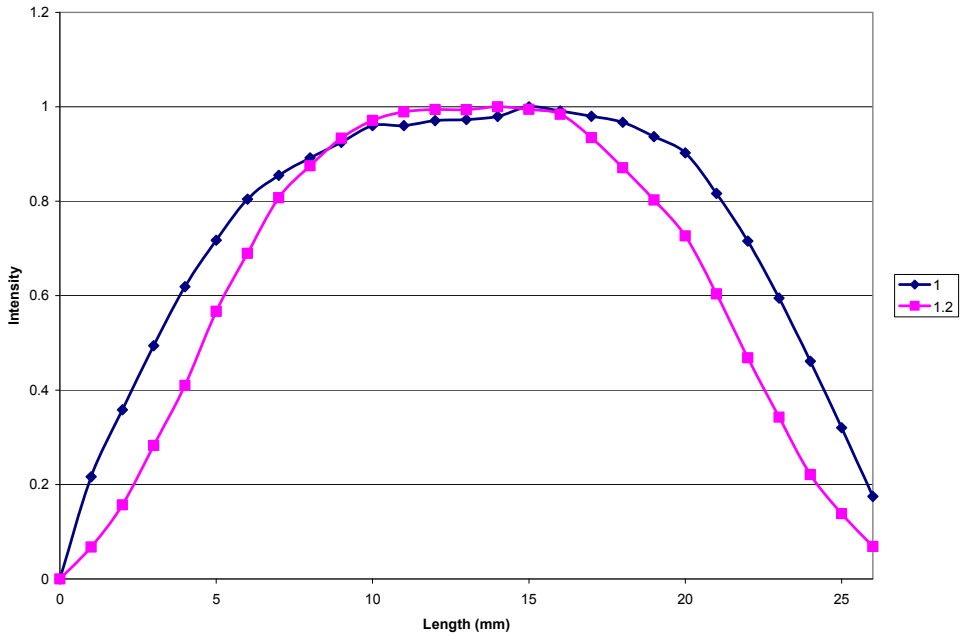

Fig. 55. Spatial profile for the Hencken flame

The shape of the graph is exactly as expected from the Hencken flame. As the laser sheet moves outside of the beam, the intensity sharply decreases.

V. Conclusions

5.1 Overview of Project

The major construction in the combustion facility at AFIT is complete and testing on the infinite radius sectional UCC is ready to begin. The actual combustion rig has been delivered and installed with all fuel, air, and instrumentation lines. The control methods for the mass flow and the temperature of the rig air have been tested and properly controlled. The emissions collection devices have all been wired, tested, and validated and are also ready for use. The JP-8 jet fuel has been delivered and has been properly connected to the ISCO fuel pumps. All ventilation is in place and is ready for use. Most importantly, the lab has been certified through the proper channels and it is safe to perform any combustion experiments. To summarize, every major piece of equipment has been tested and the lab is ready to begin experiments starting with the UCC sectional rig.

The unique capability of the AFIT combustion lab is the laser diagnostic system. The laser is currently configured for OH PLIF experiments. The laser beam is generated by an Nd: YAG laser at a wavelength of 1064 nm. The beam then travels through a frequency doubling unit where the wavelength is cut in half to 532 nm. The beam then travels through a half waveplate and polarizer to reduce the power of the laser entering the dye laser. In the current setup, the ND6000 dye laser tunes the beam to approximately 568 nm. The beam then leaves the dye laser and the wavelength cut in half by the frequency conversion unit. The beam leaves the FCU at approximately 284 nm where it is changed from a circular beam to a thin sheet using a cylindrical and spherical lens.

For this experiment the laser sheet was sent through a Hencken flame. The reason for using the Hencken flame is to calibrate the laser system on a flame where the OH concentrations and flame temperature are well known. Intensity data was compared to the theoretical equilibrium OH concentrations in the flame. The experimental data mirrored the theoretical data very well for the fuel lean equivalence ratios but had some error with the fuel rich ratios. The most likely cause for this error was the height above the top of the Hencken burner that the measurements were taken. The temperature of the flame was also calculated by determining experimental intensity ratios between different wavelengths and comparing it to the LIFBASE peak ratios between wavelengths. The experimental temperatures were low compared to the theoretical equilibrium temperatures. This too was most likely caused by the height above the top of the burner that the data was taken.

In conclusion, the data from the Hencken burner proves the laser system is calibrated and is working properly. The error in the concentration and temperature data was most likely due to the location of the beam in the Hencken flame and not the laser system. The AFIT combustion lab is now fully functional and ready for operation.

5.2 Future Work and Recommendations

Since there was error in the Hencken data, it may be desired to re-acquire and analyze Hencken data closer to the top of the burner. Being closer to the top of the burner should reduce some of the error in the experimental results.

The next step for the lab is to light the infinite radius sectional UCC rig. To prepare for this, the CAI emissions test bench needs to be calibrated and brought online.

The span gases for the CAI test bench were just delivered and calibration can begin at any time.

Once the straight section UCC is running, the quartz windows need to be placed in the rig so that OH LIF can begin on the UCC rig. Construction on the curved section should begin as soon as possible because it should be ready for testing fairly soon.

Appendix A: Mass Flow Tables for the Main Air Line

Table 8. Mass flow rates for the main air line

	kg/m	kg/sec	g/m	g/sec	lb/min	lb/sec
1	0.070	0.00117	70	1.167	0.154	0.00257
2	0.140	0.00233	140	2.333	0.309	0.00514
3	0.210	0.00350	210	3.500	0.463	0.00772
4	0.280	0.00467	280	4.667	0.617	0.01029
5	0.350	0.00583	350	5.833	0.772	0.01286
6	0.420	0.00700	420	7.000	0.926	0.01543
7	0.490	0.00817	490	8.167	1.080	0.01800
8	0.560	0.00933	560	9.333	1.235	0.02058
9	0.630	0.01050	630	10.500	1.389	0.02315
10	0.700	0.01167	700	11.667	1.543	0.02572
11	0.770	0.01283	770	12.833	1.698	0.02829
12	0.840	0.01400	840	14.000	1.852	0.03086
13	0.910	0.01517	910	15.167	2.006	0.03344
14	0.980	0.01633	980	16.333	2.161	0.03601
15	1.050	0.01750	1050	17.500	2.315	0.03858
16	1.120	0.01867	1120	18.667	2.469	0.04115
17	1.190	0.01983	1190	19.833	2.624	0.04373
18	1.260	0.02100	1260	21.000	2.778	0.04630
19	1.330	0.02217	1330	22.167	2.932	0.04887
20	1.400	0.02333	1400	23.333	3.086	0.05144
21	1.470	0.02450	1470	24.500	3.241	0.05401
22	1.540	0.02567	1540	25.667	3.395	0.05659
23	1.610	0.02683	1610	26.833	3.549	0.05916
24	1.680	0.02800	1680	28.000	3.704	0.06173
25	1.750	0.02917	1750	29.167	3.858	0.06430
26	1.820	0.03033	1820	30.333	4.012	0.06687
27	1.890	0.03150	1890	31.500	4.167	0.06945
28	1.960	0.03267	1960	32.667	4.321	0.07202
29	2.030	0.03383	2030	33.833	4.475	0.07459
30	2.100	0.03500	2100	35.000	4.630	0.07716
31	2.170	0.03617	2170	36.167	4.784	0.07973
32	2.240	0.03733	2240	37.333	4.938	0.08231
33	2.310	0.03850	2310	38.500	5.093	0.08488
34	2.380	0.03967	2380	39.667	5.247	0.08745
35	2.450	0.04083	2450	40.833	5.401	0.09002
36	2.520	0.04200	2520	42.000	5.556	0.09259
37	2.590	0.04317	2590	43.167	5.710	0.09517
38	2.660	0.04433	2660	44.333	5.864	0.09774
39	2.730	0.04550	2730	45.500	6.019	0.10031
40	2.800	0.04667	2800	46.667	6.173	0.10288
41	2.870	0.04783	2870	47.833	6.327	0.10545
42	2.940	0.04900	2940	49.000	6.482	0.10803
43	3.010	0.05017	3010	50.167	6.636	0.11060
44	3.080	0.05133	3080	51.333	6.790	0.11317
45	3.150	0.05250	3150	52.500	6.945	0.11574
46	3.220	0.05367	3220	53.667	7.099	0.11832
47	3.290	0.05483	3290	54.833	7.253	0.12089
48	3.360	0.05600	3360	56.000	7.408	0.12346
49	3.430	0.05717	3430	57.167	7.562	0.12603
50	3.500	0.05833	3500	58.333	7.716	0.12860
51	3.57	0.05950	3570	59.500	7.871	0.13118
52	3.64	0.06067	3640	60.667	8.025	0.13375
53	3.71	0.06183	3710	61.833	8.179	0.13632
54	3.78	0.06300	3780	63.000	8.334	0.13889
55	3.85	0.06417	3850	64.167	8.488	0.14146
56	3.92	0.06533	3920	65.333	8.642	0.14404
57	3.99	0.06650	3990	66.500	8.796	0.14661
58	4.06	0.06767	4060	67.667	8.951	0.14918
59	4.13	0.06883	4130	68.833	9.105	0.15175
60	4.2	0.07000	4200	70.000	9.259	0.15432
61	4.27	0.07117	4270	71.167	9.414	0.15690
62	4.34	0.07233	4340	72.333	9.568	0.15947
63	4.41	0.07350	4410	73.500	9.722	0.16204
64	4.48	0.07467	4480	74.667	9.877	0.16461
65	4.55	0.07583	4550	75.833	10.031	0.16718
66	4.62	0.07700	4620	77.000	10.185	0.16976
67	4.69	0.07817	4690	78.167	10.340	0.17233
68	4.76	0.07933	4760	79.333	10.494	0.17490
69	4.83	0.08050	4830	80.500	10.648	0.17747
70	4.9	0.08167	4900	81.667	10.803	0.18004
71	4.97	0.08283	4970	82.833	10.957	0.18262
72	5.04	0.08400	5040	84.000	11.111	0.18519
73	5.11	0.08517	5110	85.167	11.266	0.18776
74	5.18	0.08633	5180	86.333	11.420	0.19033
75	5.25	0.08750	5250	87.500	11.574	0.19291
76	5.32	0.08867	5320	88.667	11.729	0.19548
77	5.39	0.08983	5390	89.833	11.883	0.19805
78	5.46	0.09100	5460	91.000	12.037	0.20062
79	5.53	0.09217	5530	92.167	12.192	0.20319
80	5.6	0.09333	5600	93.333	12.346	0.20577
81	5.67	0.09450	5670	94.500	12.500	0.20834
82	5.74	0.09567	5740	95.667	12.655	0.21091
83	5.81	0.09683	5810	96.833	12.809	0.21348
84	5.88	0.09800	5880	98.000	12.963	0.21605
85	5.95	0.09917	5950	99.167	13.118	0.21863
86	6.02	0.10033	6020	100.333	13.272	0.22120
87	6.09	0.10150	6090	101.500	13.426	0.22377
88	6.16	0.10267	6160	102.667	13.581	0.22634
89	6.23	0.10383	6230	103.833	13.735	0.22891
90	6.3	0.10500	6300	105.000	13.889	0.23149
91	6.37	0.10617	6370	106.167	14.044	0.23406
92	6.44	0.10733	6440	107.333	14.198	0.23663
93	6.51	0.10850	6510	108.500	14.352	0.23920
94	6.58	0.10967	6580	109.667	14.506	0.24177
95	6.65	0.11083	6650	110.833	14.661	0.24435
96	6.72	0.11200	6720	112.000	14.815	0.24692
97	6.79	0.11317	6790	113.167	14.969	0.24949
98	6.86	0.11433	6860	114.333	15.124	0.25206
99	6.93	0.11550	6930	115.500	15.278	0.25463
100	7	0.11667	7000	116.667	15.432	0.25721

Appendix B: Mass Flow Tables for Secondary Air Line

Table 9. Mass flow rates for the secondary air line

	kg/m	kg/sec	g/m	g/sec	lb/min	lb/sec
1	0.020	0.00033	20	0.333	0.044	0.00073
2	0.040	0.00067	40	0.667	0.088	0.00147
3	0.060	0.00100	60	1.000	0.132	0.00220
4	0.080	0.00133	80	1.333	0.176	0.00294
5	0.100	0.00167	100	1.667	0.220	0.00367
6	0.120	0.00200	120	2.000	0.265	0.00441
7	0.140	0.00233	140	2.333	0.309	0.00514
8	0.160	0.00267	160	2.667	0.353	0.00588
9	0.180	0.00300	180	3.000	0.397	0.00661
10	0.200	0.00333	200	3.333	0.441	0.00735
11	0.220	0.00367	220	3.667	0.485	0.00808
12	0.240	0.00400	240	4.000	0.529	0.00882
13	0.260	0.00433	260	4.333	0.573	0.00955
14	0.280	0.00467	280	4.667	0.617	0.01029
15	0.300	0.00500	300	5.000	0.661	0.01102
16	0.320	0.00533	320	5.333	0.705	0.01176
17	0.340	0.00567	340	5.667	0.750	0.01249
18	0.360	0.00600	360	6.000	0.794	0.01323
19	0.380	0.00633	380	6.333	0.838	0.01396
20	0.400	0.00667	400	6.667	0.882	0.01470
21	0.420	0.00700	420	7.000	0.926	0.01543
22	0.440	0.00733	440	7.333	0.970	0.01617
23	0.460	0.00767	460	7.667	1.014	0.01690
24	0.480	0.00800	480	8.000	1.058	0.01764
25	0.500	0.00833	500	8.333	1.102	0.01837
26	0.520	0.00867	520	8.667	1.146	0.01911
27	0.540	0.00900	540	9.000	1.191	0.01984
28	0.560	0.00933	560	9.333	1.235	0.02058
29	0.580	0.00967	580	9.667	1.279	0.02131
30	0.600	0.01000	600	10.000	1.323	0.02205
31	0.620	0.01033	620	10.333	1.367	0.02278
32	0.640	0.01067	640	10.667	1.411	0.02352
33	0.660	0.01100	660	11.000	1.455	0.02425
34	0.680	0.01133	680	11.333	1.499	0.02499
35	0.700	0.01167	700	11.667	1.543	0.02572
36	0.720	0.01200	720	12.000	1.587	0.02646
37	0.740	0.01233	740	12.333	1.631	0.02719
38	0.760	0.01267	760	12.667	1.676	0.02793
39	0.780	0.01300	780	13.000	1.720	0.02866
40	0.800	0.01333	800	13.333	1.764	0.02940
41	0.820	0.01367	820	13.667	1.808	0.03013
42	0.840	0.01400	840	14.000	1.852	0.03086
43	0.860	0.01433	860	14.333	1.896	0.03160
44	0.880	0.01467	880	14.667	1.940	0.03233
45	0.900	0.01500	900	15.000	1.984	0.03307
46	0.920	0.01533	920	15.333	2.028	0.03380
47	0.940	0.01567	940	15.667	2.072	0.03454
48	0.960	0.01600	960	16.000	2.116	0.03527
49	0.980	0.01633	980	16.333	2.161	0.03601
50	1.000	0.01667	1000	16.667	2.205	0.03674
51	1.02	0.01700	1020	17.000	2.249	0.03748
52	1.04	0.01733	1040	17.333	2.293	0.03821
53	1.06	0.01767	1060	17.667	2.337	0.03895
54	1.08	0.01800	1080	18.000	2.381	0.03968
55	1.1	0.01833	1100	18.333	2.425	0.04042
56	1.12	0.01867	1120	18.667	2.469	0.04115
57	1.14	0.01900	1140	19.000	2.513	0.04189
58	1.16	0.01933	1160	19.333	2.557	0.04262
59	1.18	0.01967	1180	19.667	2.601	0.04336
60	1.2	0.02000	1200	20.000	2.646	0.04409
61	1.22	0.02033	1220	20.333	2.690	0.04483
62	1.24	0.02067	1240	20.667	2.734	0.04556
63	1.26	0.02100	1260	21.000	2.778	0.04630
64	1.28	0.02133	1280	21.333	2.822	0.04703
65	1.3	0.02167	1300	21.667	2.866	0.04777
66	1.32	0.02200	1320	22.000	2.910	0.04850
67	1.34	0.02233	1340	22.333	2.954	0.04924
68	1.36	0.02267	1360	22.667	2.998	0.04997
69	1.38	0.02300	1380	23.000	3.042	0.05071
70	1.4	0.02333	1400	23.333	3.086	0.05144
71	1.42	0.02367	1420	23.667	3.131	0.05218
72	1.44	0.02400	1440	24.000	3.175	0.05291
73	1.46	0.02433	1460	24.333	3.219	0.05365
74	1.48	0.02467	1480	24.667	3.263	0.05438
75	1.5	0.02500	1500	25.000	3.307	0.05512
76	1.52	0.02533	1520	25.333	3.351	0.05585
77	1.54	0.02567	1540	25.667	3.395	0.05659
78	1.56	0.02600	1560	26.000	3.439	0.05732
79	1.58	0.02633	1580	26.333	3.483	0.05806
80	1.6	0.02667	1600	26.667	3.527	0.05879
81	1.62	0.02700	1620	27.000	3.572	0.05953
82	1.64	0.02733	1640	27.333	3.616	0.06026
83	1.66	0.02767	1660	27.667	3.660	0.06099
84	1.68	0.02800	1680	28.000	3.704	0.06173
85	1.7	0.02833	1700	28.333	3.748	0.06246
86	1.72	0.02867	1720	28.667	3.792	0.06320
87	1.74	0.02900	1740	29.000	3.836	0.06393
88	1.76	0.02933	1760	29.333	3.880	0.06467
89	1.78	0.02967	1780	29.667	3.924	0.06540
90	1.8	0.03000	1800	30.000	3.968	0.06614
91	1.82	0.03033	1820	30.333	4.012	0.06687
92	1.84	0.03067	1840	30.667	4.057	0.06761
93	1.86	0.03100	1860	31.000	4.101	0.06834
94	1.88	0.03133	1880	31.333	4.145	0.06908
95	1.9	0.03167	1900	31.667	4.189	0.06981
96	1.92	0.03200	1920	32.000	4.233	0.07055
97	1.94	0.03233	1940	32.333	4.277	0.07128
98	1.96	0.03267	1960	32.667	4.321	0.07202
99	1.98	0.03300	1980	33.000	4.365	0.07275
100	2	0.03333	2000	33.333	4.409	0.07349

Appendix C: Bundle Diagram

Top Bundle

	Color	Gas	Name	Concentration	
Blue		H_2/He	Hydrogen/Helium Blend	40%/60%	S1
Green		C_2H_4	Ethylene		
Red		None			
Plain	None	None			
Yellow		No_x	Nitrous Oxide	High	S2
Black		C_3H_8	Propane	High	S2
White		None			

Bottom Bundle

	Color	Gas	Name	Concentration	
Blue		CO	Carbon Monoxide	High	S2
Green		CO	Carbon Monoxide	Low	S1
Red		CO_2	Carbon Dioxide	High	S2
Plain	None	CO_2	Carbon Dioxide	Low	S1
Yellow		N_2	Nitrogen		
Black		O_2	Oxygen		S1
White		Zero Air	Air		

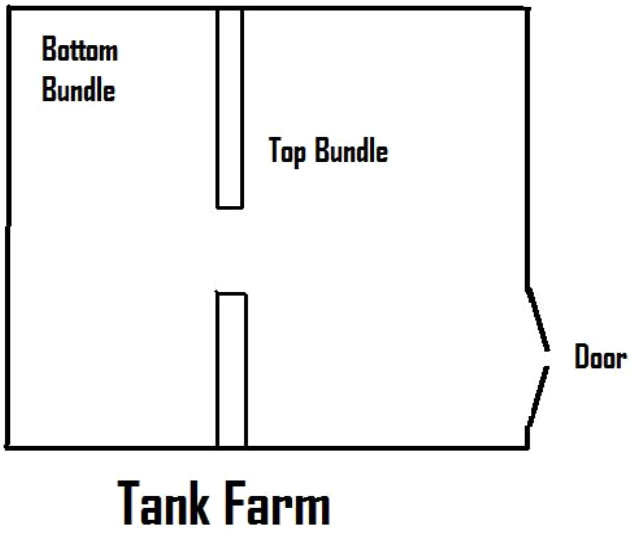

Fig. 56. Bundle diagram

Appendix D: STANJAN Data for Hydrogen-Air Flame

Table 10. Mole fractions of products in a hydrogen-air flame

	0.2	0.3	0.4	0.5	0.6	0.7	0.8	0.9	0.95	1	1.05	1.1	1.2	1.3	1.4	1.5
H	3.11E-16	8.55E-12	3.70E-09	2.11E-07	3.81E-06	3.33E-05	1.78E-04	6.70E-04	1.15E-03	1.80E-03	2.47E-03	3.00E-03	3.45E-03	3.41E-03	3.14E-03	2.79E-03
O	5.18E-12	7.03E-09	4.69E-07	7.12E-06	4.59E-05	1.68E-04	3.98E-04	6.18E-04	6.31E-04	5.42E-04	3.92E-04	2.56E-04	1.06E-04	4.71E-05	2.22E-05	1.10E-05
N	2.29E-24	2.12E-18	4.48E-15	1.37E-12	5.74E-11	8.89E-10	6.87E-09	3.05E-08	5.18E-08	7.36E-08	8.51E-08	8.29E-08	6.12E-08	4.02E-08	2.54E-08	1.59E-08
H_2	1.51E-12	3.08E-09	2.98E-07	6.54E-06	6.22E-05	3.53E-04	1.45E-03	4.96E-03	8.82E-03	1.53E-02	2.50E-02	3.74E-02	6.54E-02	9.36E-02	1.21E-01	1.47E-01
OH	1.91E-08	2.43E-06	4.17E-05	2.69E-04	9.74E-04	2.44E-03	4.60E-03	6.67E-03	7.12E-03	6.84E-03	5.90E-03	4.76E-03	2.97E-03	1.90E-03	1.25E-03	8.36E-04
CO	2.97E-15	1.08E-11	1.35E-09	3.30E-08	3.26E-07	1.85E-06	7.34E-06	2.29E-05	3.78E-05	5.87E-05	8.34E-05	1.07E-04	1.39E-04	1.57E-04	1.67E-04	1.72E-04
NO	1.24E-05	1.54E-04	6.46E-04	1.58E-03	2.77E-03	3.93E-03	4.55E-03	4.17E-03	3.53E-03	2.66E-03	1.81E-03	1.19E-03	5.34E-04	2.68E-04	1.45E-04	8.29E-05
O2	1.61E-01	1.38E-01	1.16E-01	9.42E-02	7.30E-02	5.24E-02	3.30E-02	1.62E-02	9.55E-03	4.81E-03	2.14E-03	9.33E-04	2.18E-04	6.59E-05	2.35E-05	9.37E-06
H_2O	8.06E-02	1.19E-01	1.55E-01	1.90E-01	2.23E-01	2.55E-01	2.83E-01	3.08E-01	3.17E-01	3.24E-01	3.26E-01	3.26E-01	3.19E-01	3.11E-01	3.03E-01	2.94E-01
CO_2	3.22E-04	3.16E-04	3.10E-04	3.04E-04	2.98E-04	2.91E-04	2.80E-04	2.58E-04	2.40E-04	2.16E-04	1.87E-04	1.60E-04	1.19E-04	9.34E-05	7.63E-05	6.44E-05
N_2	7.58E-01	7.43E-01	7.28E-01	7.14E-01	7.00E-01	6.86E-01	6.72E-01	6.59E-01	6.52E-01	6.44E-01	6.36E-01	6.27E-01	6.08E-01	5.89E-01	5.72E-01	5.55E-01

Table 11. PPM of products in a hydrogen-air flame

	0.2	0.3	0.4	0.5	0.6	0.7	0.8	0.9	0.95	1	1.05	1.1	1.2	1.3	1.4	1.5
H	0.00	0.00	0.00	0.21	3.81	33.28	178.47	670.10	1152.20	1796.80	2471.70	2996.30	3452.50	3407.60	3139.50	2787.80
O	0.00	0.01	0.47	7.12	45.93	167.96	397.75	617.82	631.40	541.88	391.55	256.27	106.16	47.06	22.24	11.01
N	0.00	0.00	0.00	0.00	0.00	0.00	0.01	0.03	0.05	0.07	0.09	0.08	0.06	0.04	0.03	0.02
H_2	0.00	0.00	0.30	6.54	62.17	353.47	1454.90	4958.90	8817.60	15286.00	25039.00	37443.00	65368.00	93577.00	120740.00	146580.00
OH	0.02	2.43	41.67	268.66	974.35	2440.20	4602.30	6671.50	7120.30	6837.90	5900.40	4762.10	2973.10	1897.20	1245.70	835.94
CO	0.00	0.00	0.00	0.03	0.33	1.85	7.34	22.95	37.80	58.72	83.45	106.73	139.46	157.38	166.93	171.77
NO	12.41	154.37	646.05	1576.20	2773.70	3930.50	4546.50	4173.90	3527.80	2662.10	1813.60	1185.90	534.32	268.18	145.35	82.92
O2	161230.00	138220.00	115910.00	94166.00	72961.00	52406.00	33034.00	16170.00	9545.50	4810.00	2136.50	933.26	217.70	65.87	23.55	9.37
H_2O	80619.00	118540.00	154970.00	189900.00	223200.00	254520.00	283200.00	307720.00	317240.00	323700.00	326310.00	325620.00	319450.00	311290.00	302810.00	294460.00
CO_2	322.48	316.11	309.98	304.03	298.00	290.84	279.71	258.25	240.26	215.92	187.44	160.13	119.22	93.40	76.35	64.41
N_2	757810.00	742770.00	728130.00	713770.00	699690.00	685860.00	672290.00	658740.00	651680.00	644090.00	635670.00	626540.00	607640.00	589200.00	571630.00	555000.00

Appendix E: Laboratory Start-Up and Shutdown Procedures

Lab Equipment Start-Up:

1. Turn ON valve feeding black air tank for instrument air
2. Turn ON computer
    a. Open LabView
    b. Open "Combustion Lab- Anderson Final.vi"
3. Turn ON power strip in back of computer cabinet (powers the DC supply, SCXI 1100 and DAQPad 6508)
4. Turn ON DAQ pad
5. Press "Run" on "Combustion Lab- Anderson Final.vi"
    a. Listen for fuel pumps to turn on (takes 5 sec)
6. Wait until pressure in control valve to IPT^2 reads 20-40psi and control valve to other equipment reads80-90psi
7. Turn on "Equip" switch

Hencken Flame Start-Up:

1. Turn on Fuel, Air, and Nitrogen in tank farm
2. Open valves for Fuel, Air, and Nitrogen on wall behind MOKON machine
3. Set desired mass flow rates on flow controller
    a. Turn "On" controller
    b. Turn "Display Channel" to desired channel
        i. Channel 1- Fuel
        ii. Channel 2- Air
        iii. Channel 3- CO-Flow (Nitrogen)
    c. Push Up and Hold "Set Pt."
    d. Turn screw to desired percentage
    e. Desired Equivalence Ratios for Hydrogen can be found in "Equivalence Ratios for H2.xls" on desktop
4. Turn On "Fan" switch
5. Click On "Ethylene and Air Valves" and "Fuel Line Purge" toggle switch in LabView control panel
6. Turn On Channel 2 (Air) on mass flow controller and let stabilize
7. Turn On Channel 1 (Fuel) on mass flow controller
8. Light Flame
9. Once lit, turn On Channel 3 (CO-Flow) on mass flow controller
10. Equivalence ratios may be changed on the mass flow controller during operation

UCC Start-Up Procedure

1. Run all steps in "Lab Equipment Start-Up" above
2. Turn on all bottles in the tank farm
3. Open manual ball valves on main and secondary rig air lines
4. Turn ON main and secondary Gaumer heater circuit breakers
    a. Turn the black lever to ON

    b. Push the green button
5. Turn ON the “Fan” switch to turn on the exhaust
6. Set the desired main and secondary flow rates on the LabView control screen
7. Turn ON the main and secondary air lines on the control screen
    a. It will take a few seconds for the air to reach a steady state condition
8. Once air is running, set the desired air line heater temperatures on the control screen
    a. It will take approximately 30 mins for the rig to heat up
9. Turn ON Mokon oil machine
    a. Check fluid level
    b. Make sure bypass valve is open
    c. Open chiller lines and ensure they are running
    d. Turn Power ON
    e. Press and Hold the “Start” button for 10 sec
    f. Set temperature to 350°F
    g. Check and make sure discharge pressure is below 40 psi
    h. Close the bypass valve to allow the oil to reach the probe
    i. Hold down the “Purge” button for a couple mins to get the air out of the lines
    j. Make sure pressure does not get too high
    k. It takes about 15 mins for the probe to heat up
10. Turn on California Analytical Instruments gas analyzer
    a. Check that the VI reading match the analyzer output
    b. Make sure emissions temperature is set to 340°F at control station
    c. Make sure emissions temperature control is set to 350°F at gas analyzer
    d. Make sure emissions filter is set to 200°F at gas analyzer
    e. Make sure pressure, temperature, and humidistat readings are reasonable
11. Open valves for C_2H_8, Air, and Nitrogen on wall behind MOKON machine
12. Set desired mass flow rates on flow controller
    a. Turn “On” controller
    b. Turn “Display Channel” to desired channel
        i. Channel 1- Fuel
        ii. Channel 2- Air
    c. Push Up and Hold “Set Pt.”
    d. Turn screw to desired percentage
13. Click ON “Ethelyene and Air Valves” in VI
11. Turn On Channel 2 (Air) on mass flow controller and let stabilize
12. Turn On Channel 1 (Fuel) on mass flow controller
14. Turn on “Ignitor”
15. Once lit, turn off “Ignitor”
16. Open manual fuel line valve at combustor stand
17. Set the desired JP-8 fuel flow rates
18. Turn ON the “Fuel Valve” on the VI
19. Turn ON the “Fuel Pump” switch at the VI

20. Once the combustor is ignited turn OFF “Ethylene and Air Valve”
21. Turn OFF Channel 1 and Channel 2 on mass flow controller
22. Turn OFF Mass Flow Controller
23. Change air and fuel flow to desired settings
24. Proceed with experiment

UCC Shutdown

1. Turn OFF Fuel Pumps
2. Turn OFF “Fuel Valve”
3. Set air line heater temperatures to 0
    a. It will take at least 30 mins for the heaters to cool down
    b. Do NOT turn air or heaters off until below 150°F
4. Turn ON “Fuel Line Purge”
5. Once all fuel has been purged out of the system, turn OFF “Fuel Line Purge”
6. Turn ON “Probe Purge”
7. Once emission line is purged, turn OFF “Probe Purge”
8. Turn off California Analytical Instruments analyzer
9. Turn Mokon machine temperature to 0
    a. It will take at least 15 mins for the Mokon machine to cool down
    b. Do NOT turn off machine until below 150°F
10. Once air temperatures for main and secondary line are below 150°F, click OFF main and secondary air lines
11. Manually turn OFF electric heater circuit breakers
12. Once Mokon machine is below 150°F turn OFF machine
    a. Close the chiller lines
    b. Turn Power OFF
13. Close the ethylene, air, and nitrogen valves at the wall behind the Mokon machine
14. Close all bottles in the tank farm
15. Turn OFF “Fan”
16. Proceed to “Lab Shutdown”

Hencken Flame Shutdown:

1. While running- turn fuel, air, and nitrogen off out in tank farm
2. Turn off mass flow controller
3. Click off the “Fuel and Air Valve” and “Fuel Probe Purge” toggle switch in LabView control panel
4. Close valves for Fuel, Air, and Nitrogen on wall behind MOKON machine
5. Turn off fan
6. Proceed to “Lab shutdown”

Lab Shutdown:

1. Turn off “Equip” switch
2. Push “Stop” on Labview
3. Turn off DAQ pad

4. Turn off power strip in back of cabinet
5. Turn off air valve to black tank

Appendix F: Laser and Camera Start-up and Shutdown Procedure

Laser Start-up procedure

Safety

1. Secure entrances to the laboratory
2. Activate laser warning lights
3. Check to ensure that all personnel have the proper PPE
4. Check to ensure that all personnel have proper safety training
5. Check to ensure that all beam paths are initially blocked
6. Check to ensure that beam paths are enclosed or away from operator vision

Laser (from a complete Power Down)

1. Check water level and flow to YAG power supply
2. Turn keyswitch on YAG power supply

Periodic Maintenance

1. Check dye in circulator, refill with methanol if necessary to 5-10mm below the bottom of the tube
2. Check water level in YAG power supply
3. Run the laser every 1 to 2 weeks
4. Clean 45 degree optics every day if running or every week if not running

Laser Operation (Day to Day):

1. Turn on dye pump
2. Click the “enable” button on the YAG keypad
3. Allow amber simmer lightes on the YAG keypad to stop blinking
4. Turn “osc” flashlamp energy to 5 on the YAG keypad
5. Double click “Trigger” software on the computer desktop
6. Click “File” the “Open” and open text file- ex: “AFIT 1 YAG 1 Camera”
7. Click “Program” button to load settings- it’s the button between “H” and “Reset”
8. Click “Enable” on Channel A of “Trigger” software (if not already enabled)
9. Allow YAG laser to warm up for 20 minutes
10. Click “Enable” on Channel C of computer control software to turn on Q-switch
11. After checking beam path, turn up “osc” flashlamp energy to full power
12. Set delay in Channel C of “Trigger” software to 180 microseconds and click Apply and Enable
13. Open Wavemeter software, click start, and set signal to “Pulsed”
14. Check wavemeter reading and adjust dye laser wavelength to desired wavelength using ND6000 software

Camera Start-up:

1. Turn On computer that controls camera
2. Open WinView
3. Click “Restore last settings”
4. Click “Experiment Setup”
5. Turn gain to 0
6. Click “Focus” and check alignment, focus, and pulse timing using a business card
7. Change gain back to ~255
8. In “Experiment Setup” perform desired experiment and push “Acquire” to begin

Shutdown Procedures:

Camera:

1. End current experiment
2. Close WinView if desired

Laser Shutdown:

1. Click “Disable” on Channel C of “Trigger” software
2. Turn “osc” flashlamp energy to 0 on YAG keypad
3. Allow water to keep running for at least 10 to 15 mins
4. Push “Stop” on YAG keypad
5. Turn off dye pump
6. Close software if desired

References

1. Sirignano, W.A., and Liu, F., "Performance Increases for Gas-Turbine Engines Through Combustion Inside the Turbine," Journal of Propulsion and Power, 15:1 pp. 111-118 : 1999.
2. Zelina, J., G.J. Sturgess, and D.T. Shouse. "The Behaviour of an Ultra-Compact Combustor (UCC) Base on Centrifugally-Enhanced Turbulent Burning Rates," 40th AIAA/ASME/SAE/ASEE Joint Propulsion Conference and Exhibit, AIAA 2004-3541, Fort Lauderdale, FL: July 2004.
3. Greenwood, Roger T., "Numerical Analysis and Optimization of the Ultra Compact Combustor," MS Thesis, AFIT/GAE/ENY/05-M10, Graduate School of Engineering and Management, Air Force Institute of Technology (AU), Wright Patterson AFB, OH: March 2005.
4. Dittman, E. R. "Design, Build, and Validation of a Small Scale Combustion Chamber Testing Facility," MS Thesis, AFIT/GAE/ENY/06-M06, Graduate School of Engineering, Air Force Institute of Technology (AU), WPAFB, OH: March 2006.
5. Anderson, W. S. "Design, Construction, and validation of the AFIT Small Scale Combustion Facility and Sectional Model of the Ultra-Compact Combustor," MS Thesis, AFIT/GAE/ENY/07-M01, Graduate School of Engineering, Air Force Institute of Technology (AU), WPAFB, OH. March 2006.
6. Barnard, J. A. and J. N. Bradley, *Flame and Combustion* (Second Edition), New York: Chapman and Hall, 1985.
7. Wilson, D. G., & Korakianitis, T. *The Design of High-Efficiency Turbomachinery and Gas Turbines*, 2nd Ed. Upper Saddle River, Prentice Hall, New Jersey, 1998.
8. Zelina, J., R.T. Greenwood, and D.T. Shouse, "Operability and Efficiency Performance of Ultra-Compact, High Gravity (g) Combustor Concepts," Proceedings of ASME TURBO EXPO '06: 51st ASME International Gas Turbine and Aeroengine Congress and Exposition, GT2006-90119, Barcelona, Spain: May 2006
9. Roquermore, W.M., Dale Shouse, Dave Burrus, and others, "Trapped Vortex Combustor Concept of Gas Turbine Engines," 39th AIAA Aerospace Sciences Meeting & Exhibit, AIAA 2001-0483, Reno, NV: January 2001.
10. Lewis, George D. "Swirling Flow Combustion—Fundamentals and Application," 9th AIAA/SAE Propulsion Converence, AIAA 73-1250. Las Vegas, NV: 1973.
11. Lewis, George D. "Centrifugal-Force Effects on Combustion," Fourteenth Symposium on Combustion, Pittsburgh, PA: The Combustion Institute, p. 413-419, 1972.
12. Yonezawa, Y., Toh, H, Goto, S., & Obata, M. "Development of the Jet-Swirl High Loading Combustor." AIAA/SAE/ASME/ASEE 26th Joint Propulsion Conference, Orlando, FL. 1990.
13. Anthenien, R. A., Mantz, R.A., Roquemore, W.M., & Sturgess, G. "Experiemental Results for a Novel, High Swirl, Ultra-Compact Combustor for Gas Turbine Engines," 2nd Joint Meeting of the United States Section of the Combustion Institute, Oakland, CA. 2001.

14. Zelina, J., Sturgess, G. J., Manour, A., & Handcock, R. D. “Fuel Injector Design for an Ultra-Compact Combustor” ISABE 2003-1089. WPAFB, OH: 2003.
15. Quaale, Ryan J., Ralph A. Anthenien, Joseph Zelina, and Jeffery Ehret, “Flow Measurments within a High Swirl Ultra Compact Combustor for Gas Turbine Engines,” ISAVE-2003-1141, WPAFB, OH: 2003
16. Zelina, J., Dale T. Shouse, and Craig Neuroth, “High-Pressure Tests of a High-g Ultra-Compact Combustor,” 41st AIAA/SAE/ASME/ASEE Joint Propulsion Converence and Exhibit, AIAA 2005-3779, Tucson, AZ: July 2005.
17. Moenter, D. S. “Design and Numerical Simulation of Two-Dimensional Ultra-Compact Combustor Model Sections for Experiemental Observation of Cavity-Vane Flow Interactions,” MS Thesis, AFIT/GAE/ENY/06-S07, Graduate School of Engineering, Air Force Institute of Technology (AU), WPAFB, OH September 2006.
18. Kohse-Hoinghaus, Katharina. “Laser Techniques for the Quantitative Detection of Reactive Intermediates in Combustion Systems”. Prog. Energy Combust. Sci, Vol 20, Great Britain, pp 203-279, 1994.
19. Eckbreth, A.C. & Stufflebeam, J. H. “CARS diagnostics for combustion and plasma processes” Materials Research Society Symposium, Process Diagnostics: Materials, Combustion, Fusion, Reno, NV. Pp 217-226. (1988).
20. Eckbreth, A.C., Bonczyk, P.A., & Verdieck, J.F. “Combustion Diagnostics by Laser Raman and Fluorescence Techniques.” Progress in Energy and Combustion Sciences, 5, p 253-322: 1979.
21. J. Luque and D.R. Crosley, “LIFBASE: Database and Spectral Simulation Program (Version 2.0.55),” SRI International Report MP 99-009 (1999)
22. Tamura, Masayuki, Pamela A. Berg, Joel E. Harrington, Jorge Luque, Jay B. Jefferies, Gregory P. Smith, and David R. Crosley. “Collisional Quenching of CH(A), OH(A), and NO(A) in Low Pressure Hydrocarbon Flames” *Combustion and Flame*, Vol 114, p 502-514, 1998.
23. Reynold, William C. “STANJAN: Equilibrium solver.” Stanford University, CA, 1995.
24. Meyer, Terry. Private Communication, AFIT Temperature Study showing the temperature dependence of various LIFBASE lines. Iowa State University, August 2007.
25. CVI Laser Product Catalog, Schott Color Glass Filters, p 317, 2007.
26. Seitzman, J.M., R. K. Hanson, P. A. DeBarber, and C. F. Hess, “Application of quantitative two-line OH planar laser-induced fluorescence for temporally resolved planar thermometry in reacting flows,” Applied Optics, Vol. 33, No. 18, June 1994.

REPORT DOCUMENTATION PAGE

Form Approved
OMB No. 074-0188

1. REPORT DATE *(DD-MM-YYYY)*	**2. REPORT TYPE**	**3. DATES COVERED** *(From – To)*
13 September 2007	**Master's Thesis**	January 2007-September 2007

4. TITLE AND SUBTITLE

VALIDATION OF THE AFIT SMALL SCALE COMBUSTION FACILITY AND OH LASER-INDUCED FLUORESCENCE OF AN ATMOSPHERIC LAMINAR PREMIXED FLAME

5a. CONTRACT NUMBER

5b. GRANT NUMBER

5c. PROGRAM ELEMENT NUMBER

6. AUTHOR(S)

Koether, Stephen J., 2nd Lt, USAF

5d. PROJECT NUMBER

5e. TASK NUMBER

5f. WORK UNIT NUMBER

7. PERFORMING ORGANIZATION NAMES(S) AND ADDRESS(S)
Air Force Institute of Technology
Graduate School of Engineering and Management (AFIT/EN)
2950 Hobson Way
WPAFB OH 45433-7765

8. PERFORMING ORGANIZATION REPORT NUMBER

AFIT/GAE/ENY/07-S03

9. SPONSORING/MONITORING AGENCY NAME(S) AND ADDRESS(ES)
AFRL/PRTC
Dr. Joseph Zelina
1790 Loop Road North
WPAFB, OH 45433
(937) 255-7487

10. SPONSOR/MONITOR'S ACRONYM(S)

11. SPONSOR/MONITOR'S REPORT NUMBER(S)

12. DISTRIBUTION/AVAILABILITY STATEMENT
APPROVED FOR PUBLIC RELEASE; DISTRIBUTION UNLIMITED.

13. SUPPLEMENTARY NOTES

14. ABSTRACT

Construction in the AFIT combustion facility is complete and the objective of this report is to explain the steps taken to make the laboratory operational. The infinite radius Ultra-Compact Combustor (UCC) sectional model has been delivered and is fully installed with all fuel, air and instrument lines. Every major system in the lab has been tested and is functioning properly. Laboratory operating procedure has been established to ensure both safety and continuity in experimental results. Finally, the lab has been certified through official safety channels and combustion experiments are underway. The unique capability of the AFIT combustion laboratory is the laser diagnostic system. The laser system has been configured for OH Laser-Induced Fluorescence (LIF) and initial experiments were performed on a premixed, laminar flame produced by a Hencken burner. The LIF methods accurately measured the OH concentration and temperature of the flame as compared to theoretical equilibrium flame data with an overall system uncertainty of approximately 2.5%. Therefore, the laser system has been calibrated and is ready for future use.

15. SUBJECT TERMS
Combustion, Combustors, Experimental, Laboratory, Laser Diagnostics, Ultra-Compact Combustor, Laser-Induced Fluorescence, Hencken

16. SECURITY CLASSIFICATION OF:			**17. LIMITATION OF ABSTRACT**	**18. NUMBER OF PAGES**	**19a. NAME OF RESPONSIBLE PERSON**
REPORT	**ABSTRACT**	**c. THIS PAGE**			Dr. Paul King, ENY
U	**U**	**U**	**UU**	97	**19b. TELEPHONE NUMBER** *(Include area code)* (937) 255-3636 x4628,

Standard Form 298 (Rev: 8-98)
Prescribed by ANSI Std. Z39-18